Kaunas University of Technology

Faculty of Mechanical Engineering and Design

Research and Development of 3D Printed Strain Sensors for Structural State and Health Monitoring

Master's Final Degree Project

Elshada Jasper

Project author

Assoc. Prof. Martynas Lendraitis

Supervisor

Kaunas, 2026

Kaunas University of Technology
Faculty of Mechanical Engineering and Design

Research and Development of 3D Printed Strain Sensors for Structural State and Health Monitoring

Master's Final Degree Project

Aeronautical Engineering (6211EX024)

Elshada Jasper
Project author

Assoc. Prof. Martynas Lendraitis
Supervisor

Prof. Artūras Keršys
Reviewer

Kaunas, 2026

Kaunas University of Technology

Faculty of Mechanical Engineering and Design

Elshada Jasper

Research and Development of 3D Printed Strain Sensors for Structural State and Health Monitoring

Declaration of Academic Integrity

I confirm the following:

1. I have prepared the final degree project independently and honestly without any violations of the copyrights or other rights of others, following the provisions of the Law on Copyrights and Related Rights of the Republic of Lithuania, the Regulations on the Management and Transfer of Intellectual Property of Kaunas University of Technology (hereinafter – University) and the ethical requirements stipulated by the Code of Academic Ethics of the University;

2. All the data and research results provided in the final degree project are correct and obtained legally; none of the parts of this project are plagiarised from any printed or electronic sources; all the quotations and references provided in the text of the final degree project are indicated in the list of references;

3. I have not paid anyone any monetary funds for the final degree project or the parts thereof unless required by the law;

4. I understand that in the case of any discovery of the fact of dishonesty or violation of any rights of others, the academic penalties will be imposed on me under the procedure applied at the University; I will be expelled from the University and my final degree project can be submitted to the Office of the Ombudsperson for Academic Ethics and Procedures in the examination of a possible violation of academic ethics.

Elshada Jasper

Confirmed electronically

Kaunas University of Technology

Faculty of Mechanical Engineering and Design

Task of the Master's Final Degree Project

Given to the student – Elshada Jasper

1. Topic of the project

Research and Development of 3D Printed Strain Sensors for Structural State and Health Monitoring

(In English)

3D spausdintų deformacijos jutiklių, skirtų konstrukcijų būklės stebėsenai, kūrimas ir tyrimai

(In Lithuanian)

2. Aim and tasks of the project

Aim: To develop a 3D printed sensor and evaluate its performance under mechanical loading through integration into an aircraft structural element for structural state and health monitoring.

Tasks:

1. To review current sensor technologies used to monitor structural behaviour under mechanical loading.
2. To design and manufacture a 3D printed sensor using conductive materials.
3. To develop an experimental setup for mechanical loading and data collection.
4. To investigate the sensor's electrical response under mechanical loading.
5. To integrate the developed sensor into an aircraft structural element and evaluate its performance under mechanical loading.

3. Main requirements and conditions

1. The sensor shall be manufactured using commercially available conductive filament materials.
2. The sensor shall be fabricated using FDM (Fused Deposition Modelling) 3D printing technology.
3. The sensor shall be compact and suitable for installation on an aircraft structural component.
4. The sensor shall demonstrate adequate strain measurement sensitivity, verified using commercially available equipment and within strain ranges representative of aircraft structural service life.

5. Additional requirements and conditions for the project, report and appendices

Not applicable

Project author	Elshada Jasper	15-02-2026
	(Name, Surname)	*(Date)*
Supervisor	Martynas Lendraitis	15-02-2026
	(Name, Surname)	*(Date)*
Head of study field programs	Artūras Keršys	15-02-2026
	(Name, Surname)	*(Date)*

Jasper, Elshada. Research and Development of 3D Printed Strain Sensors for Structural State and Health Monitoring. Master's Final Degree Project / supervisor assoc. prof. Martynas Lendraitis, Faculty of Mechanical Engineering and Design, Kaunas University of Technology.

Study field and area (study field group): Aeronautical Engineering (E14), Engineering Science.

Keywords: Structural health monitoring, strain sensor, additive manufacturing, conductive PLA, Wheatstone bridge, gauge factor.

Kaunas, 2026. 66.

Summary

In aviation, structural health monitoring relies solely on continuous sensing of the structure's behaviour to detect damage and monitor load conditions. Aircraft are subjected to cyclic and mechanical loadings in extreme environmental conditions during their operational life. Hence, detecting structural degradation early is critical for maintaining safety and airworthiness. Though conventional sensor technologies are effective, they are quite expensive, need a complex installation procedure and are very difficult to customise for complex structures. These limitations have led to the search for an alternative sensing approach that can be readily integrated into structures. Additive manufacturing poses as a suitable alternative as it enables us to fabricate the sensing elements directly within or on the structure at low cost, and with a high geometric customisation flexibility. Fused Deposition Modelling using conductive polymer filaments has emerged as a particularly accessible approach; however, the existing research has remained at the basic testing level with limited investigation of real structural integration and combined loading conditions.

This project developed and evaluated 3D printed strain sensors using the FDM technique with conductive polymer filaments. Two evaluated filaments were Protopasta Conductive Pla and Filaflex conductive TPU. The materials were evaluated in both single extrusion and integrated into a simple sensor geometry. In both cases, Protopasta PLA exhibited significantly lower resistance of approximately 275 kΩ compared to approximately 1100 kΩ for TPU-based, hence Protopasta PLA was selected as a suitable material for subsequent development.

Two full Wheatstone bridge layouts were designed and fabricated. Layout I adopted a longitudinal configuration of a total bridge resistance of 137 kΩ, while layout II adopted a more compact geometry with a total bridge resistance of 100 kΩ approximately. For establishing electrical connections, conductive thermal bonding was chosen as the method of contact, as it yields stable and repeatable measurements. Data acquisition was performed using an NI 9237 bridge input module and an NI cDAQ-9173 chassis, with signal processing carried out in MATLAB.

Both the layouts were characterised under tensile and three-point bending loading conditions using a Tinius Olsen universal testing machine. Under tensile loading, Layout II achieved a gauge factor of 1.27, compared to 0.398 for Layout I. Under three-point bending, Layout II achieved a gauge factor of 1.20, compared to 1.0 for Layout I. A temperature drift experiment from 20°C to 60°C revealed that layout II is much more thermally stable. The improved sensitivity and thermal stability of the second layout are attributed to its compact and symmetrical bridge geometry, efficient strain transfer and uniform heating distribution in the sensing elements.

The compact sensor layout was integrated into a 13-inch FPV arm and was evaluated under bending and torsional loading conditions. Three sensors were embedded at different locations along the arm. The two aligned sensors near the fixed and mid-span determine the bending strain, while one 45° orientation placed near the free end captures the shear and normal strain under torsional loading. Under cantilever bending, the sensors captured the expected strain distribution, with experimental values within approximately 10% of theoretical predictions near the fixed support and within 15–20% at mid-span. A gauge factor of approximately 1.07 was extracted for the bending sensors. Under combined bending and torsional loading, a gauge factor of 0.97 was obtained for the 45° sensor using strain superposition of bending and torsional contributions.

The results confirm that 3D printed strain gauges are a feasible and low-cost solution for structural state monitoring in lightweight UAV structures. Temperature sensitivity and fabrication repeatability remain areas requiring further investigation before deployment in real operational environments. Future work should focus on multi-specimen repeatability testing, active temperature compensation, and long-term durability evaluation under cyclic loading conditions.

Jasper, Elshada. 3D spausdintų deformacijos jutiklių skirtų konstrukcijų būklės stebėsenai kūrimas, ir tyrimai. Magistro baigiamasis projektas / doc. Martynas Lendraitis; Kauno technologijos universitetas, Mechanikos inžinerijos ir dizaino fakultetas.

Studijų kryptis ir sritis (studijų krypčių grupė): Aeronautikos inžinerija (E14), Inžinerijos mokslai.

Reikšminiai žodžiai: Konstrukcijų būklės stebėsena, deformacijos jutiklis, adityvioji gamyba, PLA, Vitstono tiltas, jautrumo koeficientas.

Kaunas, 2026. 66 p.

Santrauka

Aviacinių konstrukcijų būklės stebėjimas remiasi nuolatiniu konstrukcijos elgsenos sekimu, siekiant laiku aptikti pažeidimus ir stebėti veikiančias apkrovas. Orlaiviai per visą eksploatavimo laiką yra veikiami ciklinių ir mechaninių apkrovų, kurios kartais gali būti itin didelės. Todėl ankstyvas konstrukcijos degradacijos aptikimas yra labai svarbus skrydžių saugumui ir tinkamumui palaikyti. Nors tradicinės jutiklių technologijos yra veiksmingos, jos yra gana brangios, reikalauja sudėtingų montavimo procedūrų ir yra sunkiai pritaikomos sudėtingoms konstrukcijoms. Šie apribojimai paskatino ieškoti alternatyvių jutiklių sprendimų, kurie galėtų būti lengviau integruojami į pačias konstrukcijas.

Adityviosios gamybos technologijos yra tinkama alternatyva, nes leidžia tiesiogiai įterpti jutiklinius elementus konstrukcijos viduje arba ant jos paviršiaus mažomis sąnaudomis ir užtikrinant didelį lankstumą. Lydyto plastiko klojimo (FDM) modeliavimas naudojant laidžius polimerus tapo ypač prieinamu metodu. Tačiau esami tyrimai iš esmės apsiriboja baziniais bandymais, o realios konstrukcinės integracijos bei tyrimų, vertinančių kombinuotų apkrovų sąlygas, vis dar trūksta.

Šiame projekte buvo sukurti ir įvertinti 3D spausdinti deformacijų jutikliai, pagaminti FDM technologija naudojant laidžias polimerines gijas. Buvo tiriamos dvi medžiagos: Protopasta laidus PLA ir Filaflex laidus TPU. Medžiagos vertintos tiek pavienės ekstruzijos būdu, tiek integruotos į paprastą jutiklio geometriją. Abiem atvejais Protopasta PLA pasižymėjo žymiai mažesne varža – apie 275 kΩ, palyginti su maždaug 1100 kΩ Filaflex TPU pagrindo jutikliuose. Todėl Protopasta PLA buvo pasirinkta kaip tinkama medžiaga tolesniam jutiklių kūrimui.

Buvo suprojektuoti ir pagaminti du pilni Vitstono (Wheatstone) tiltelio išdėstymai. Pirmojo bendra tiltelio varža siekė 137 kΩ (išilginė konfigūracija), o antrojo, kompaktiškos geometrijos išdėstymo – apytiksliai 100 kΩ. Variniai laidai prie jutiklio buvo prijungti litavimo būdu, kaip įliejančią medžiagą naudojant tą patį Protopasta plastiką. Duomenų surinkimas atliktas naudojant NI 9237 tiltelio įvesties modulį ir NI cDAQ-9173 duomenų apdorojimo stotį. Signalai apdoroti MATLAB programine įranga.

Abu jutiklių išdėstymai buvo ištirti esant tempimo ir trijų taškų lenkimo apkrovoms, naudojant standartinius bandinius su įlietais jutikliais ir Tinius Olsen universalią bandymų mašiną. Esant tempimo apkrovai, antrasis išdėstymas pasiekė 1,27 jautrumo koeficientą (palyginti su 0,398 pirmuoju atveju). Esant trijų taškų lenkimui, antrasis išdėstymas pasiekė 1,20 jautrumo koeficientą (palyginti su 1,0 pirmuoju). Temperatūros pokyčio eksperimentas (nuo 20°C iki 60°C) atskleidė, kad antrasis išdėstymas yra žymiai termiškai stabilesnis. Pagerintas antrojo išdėstymo jautrumas ir

terminis stabilumas priskiriamas jo kompaktiškai bei simetriškai tiltelio geometrijai, efektyviam deformacijos perdavimui ir tolygiam jutiklio elementų šilimui.

Kompaktiškas jutiklio išdėstymas buvo integruotas į 13 colių FPV drono rėmą ir įvertintas esant lenkimo bei sukimo apkrovoms. Trys jutikliai buvo įmontuoti skirtingose vietose išilgai drono sijos. Du išilgai sijos sumontuoti jutikliai (šalia fiksuoto galo ir viduryje) nustato lenkimo deformaciją, o vienas 45° kampu orientuotas jutiklis, esantis šalia laisvojo galo, fiksuoja šlyties ir normalines deformacijas esant sukimo apkrovai. Esant grynojo lenkimo sąlygoms, jutikliai užfiksavo tikėtiną deformacijos pasiskirstymą – eksperimentinės vertės buvo apie 10% paklaidos ribose nuo teorinių prognozių šalia įtvirtinimo taško ir 15–20% paklaidos ribose vidurio ruože. Lenkimo jutikliams gautas maždaug 1,07 jautrumo koeficientas. Esant kombinuotam lenkimo ir sukimo apkrovimui, 45° jutikliui nustatytas 0,97 jautrumo koeficientas, naudojant lenkimo ir sukimo indėlių deformacijos superpoziciją.

Rezultatai patvirtina, kad 3D spausdinti deformacijų jutikliai yra perspektyvi ir ekonomiška priemonė lengvų UAV konstrukcijų būklei stebėti. Vis dėlto jautrumas temperatūrai ir gamybos atkartojamumas tebėra sritys, kuriose būtini tolesni tyrimai prieš pritaikant šiuos jutiklius realiomis eksploatavimo sąlygomis. Ateityje reikėtų daugiau dėmesio skirti pakartotiniams bandymams su didesniu bandinių kiekiu, aktyvios temperatūros kompensavimo sistemos kūrimui bei ilgalaikio patvarumo vertinimui esant ciklinėms apkrovoms.

Table of contents

List of figures

List of tables

Introduction

In aviation, where aircraft structures are continuously subjected to cyclic loads and vibrations throughout their operational life, maintaining structural integrity is vital. These factors, over time, lead to structural degradation; hence, early detection of the potential damage is crucial. The traditional methods are time-consuming, which is often conservative, labour-intensive and since components are frequently replaced based on predetermined service intervals rather than their actual structural condition. Structural Health Monitoring is a promising alternative approach, which is condition-based as sensor systems continuously monitor the structure and the loading conditions. Such systems can detect early damage and possible fatigue, which could go unnoticed during visual inspections. SHM has the potential to improve safety and operational efficiency, reduce maintenance costs. The effectiveness of SHM strongly depends on the sensing systems. However, these conventional systems are a bit expensive, have complicated installation methods and are not flexible to customise as per one's needs and requirements.

Recent advancements in additive manufacturing have opened possibilities of embedding these sensing elements directly on the structural component using the Fused Deposition Modelling technique and conductive filaments. They offer low manufacturing costs, geometric flexibility and rapid prototyping and fabrication capability.

Several studies have investigated the feasibility of fabricating sensors using the FDM technique and polymer-based conductive filaments. Research has demonstrated that they can measure strain under loading conditions and exhibit a linear electrical output. Different designs and orientations are explored to enhance sensitivity and improve temperature compensation. Despite these developments, existing research is largely limited to laboratory-scale testing on flat specimens or coupons, with limited exposure to integration into structural elements.

The novelty of this work lies in the research, development and characterisation of the 3D printed sensors. The materials are evaluated, two different layouts are designed and fabricated and are subjected to tensile and three-point bending conditions. And finally, the developed sensor was integrated into an FPV arm and experimentally evaluated under practical bending and torsional loading conditions. Therefore, this work extends further than specimen-level testing and investigates its feasibility in structural state monitoring applications.

The project aims to develop a 3D printed sensor and evaluate its performance under mechanical loading through integration into an aircraft structural element for structural state and health monitoring.

To achieve this aim, the following tasks were defined:

1. To review current sensor technologies used to monitor structural behaviour under mechanical loading.
2. To design and manufacture a 3D printed sensor using conductive materials.
3. To develop an experimental setup for mechanical loading and data collection.
4. To investigate the sensor’s electrical response under mechanical loading.
5. To integrate the developed sensor into an aircraft structural element and evaluate its performance under mechanical loading.

1. Literature Review

1.1. Structural health monitoring in aviation

In aviation, structural health monitoring is implemented to monitor the structural integrity of the aircraft continuously using permanently installed sensors and data analysis. Hence, reducing the dependence on heavy scheduled inspections and surprise failures. It is considered safer and more cost-effective for fleets throughout the life cycle [1,2]. A typical on-line SHM system architecture, illustrating the integration of sensors, data communication, signal analysis, and damage quantification, is shown in Fig. 1.

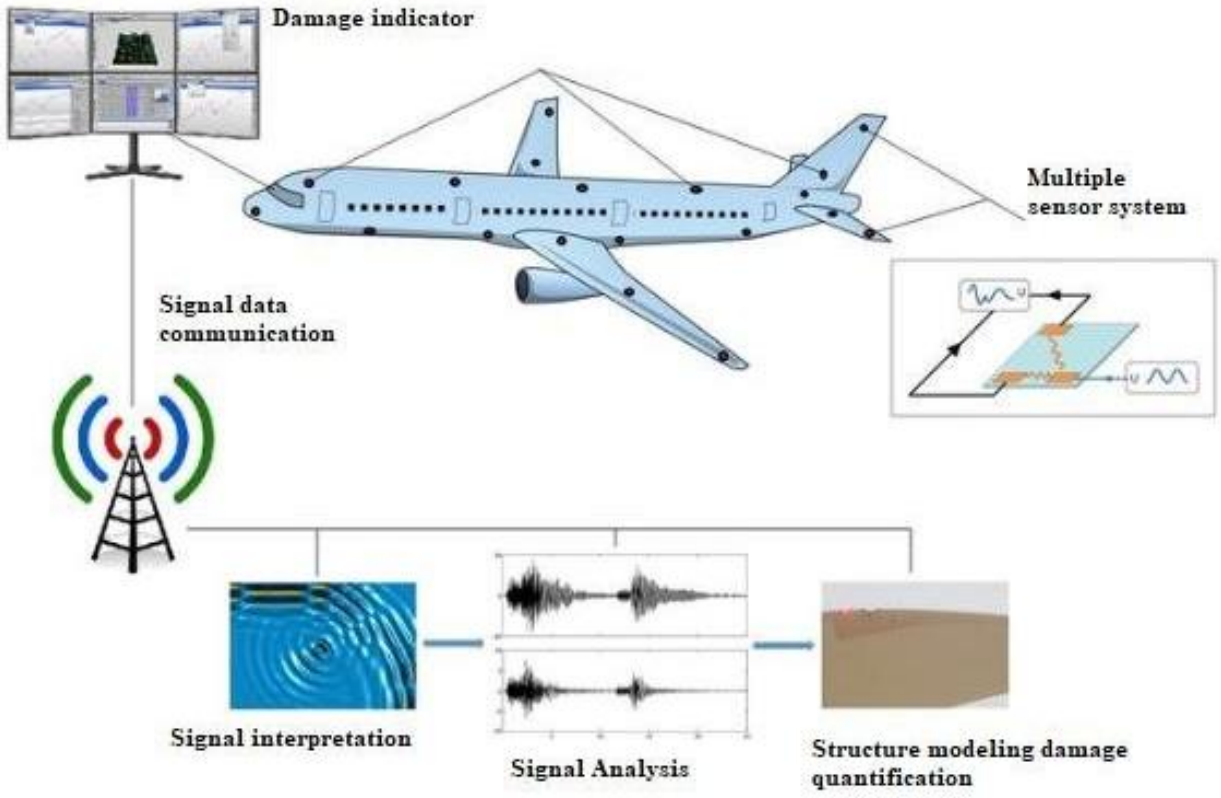

Fig. 1. On-line Structural Health Monitoring of Aircraft [3]

Aircraft structures operate in intense conditions and environments, being subjected to cyclic mechanical loads and long service durations. Over time, these conditions may lead to structural degradation such as fatigue cracking, corrosion or material deterioration, which could compromise the integrity and lead to failure. Hence, ensuring safety is the main priority in the aerospace and aviation industries.

Aircraft structural integrity, traditionally, has been maintained through scheduled inspection and maintenance programs relying on visual inspections and non-destructive evaluation techniques to identify damage. Though this approach is effective, it is often conservative and resource-intensive. Components and parts might be replaced irrespective of their actual conditions, leading to an increase in maintenance costs and aircraft downtime [4].

Structural Health Monitoring (SHM) offers an alternative approach. It is important because SHM can:

- Detect hidden or barely visible damage like early fatigue cracks, delamination that visual inspection may miss [1].
- Support continuous or frequent monitoring, shifting the focus from time-based to condition-based monitoring [2,5].
- Provide more accurate operational load histories on wings and fuselage, improving fatigue life assessment [1].
- Increase overall safety and reduce lifecycle cost [4].

With the increase in complexity of aircraft structures and operational demands in the aviation sector, SHM is gaining more attention. Despite the potential benefits and implementation of SHM in commercial aviation, there are also challenges like long-term performance under harsh environmental conditions, system reliability, certification requirements, and integration of this method of inspection in existing aircraft fleets.

The SHM systems combine multiple sensors like strain, vibration, and ultrasonic to detect, locate and also quantify damage using algorithms and sensing methods shown in Table.1.

Table 1. Common sensing methods under SHM [4-6]

SHM's role in aircraft	**Common sensing methods**
Fatigue/load monitoring of wings and fuselage	Electrical strain gauges, fiber-optic strain, optimised placement to minimise sensor count while preserving load accuracy
Crack/damage detection in metals and composites	Acoustic emission, guided Lamb waves with piezoelectric transducers, impact-echo and ultrasonics, vibration-based methods
Corrosion monitoring	Electrochemical impedance sensors, galvanic and resistance-based corrosion sensors, and chemical ion-selective sensors
Global condition assessment & diagnostics	Sensor networks with SHM algorithms, sometimes integrated with digital twins and advanced data analytics

1.1.1. Advantages and challenges of SHM in commercial aviation

Apart from its technical role in monitoring the structural integrity, SHM also carries significant importance in terms of operations for airlines and aircraft operators. Commercial aviation is very sensitive to factors like maintenance costs, aircraft availability, and schedules. Unexpected structural issues spike these factors, leading to costly downtime, delays and disruptions to the schedule. Hence, monitoring the fleet to attain prior insights into the structural condition is a valuable tool for overall improvement of maintenance and planning [1].

For this reason, SHM is gaining attention and is viewed not only as a diagnostic tool but also as a step towards predictive maintenance and digital aircraft management [2,7].

Though there is significant interest and potential for more technological progress, SHM still faces several technical, regulatory and operational challenges. Existing certification standards do not fully cover SHM systems, and new guidelines must clearly define the sensors, structures and software involved, while also addressing durability and reliability testing requirements in the aviation context [2]. Sensor survivability under high temperature, humidity, and fluid exposure remains a concern, as these conditions can degrade sensor signals over time, emphasising the need for more robust designs and qualification testing [2]. The size and complexity of sensor networks also introduce practical

challenges, as larger networks increase weight and data handling burden, driving research towards smarter and more efficient sensor placement strategies [4,9]. Finally, the upfront installation and certification costs present a significant adoption hurdle in airline operations, and must be justified through demonstrated reductions in maintenance costs and improvements in aircraft availability [1,9].

1.2. Structural sensor technologies

Structural sensor technologies are of core importance in SHM systems as they are used to obtain information on the integrity and the performance of the structure, relying on continuous or periodic data acquisition from the sensor networks. This data proves critical in detecting damage, monitoring load conditions and also in the evaluation of critical components like the wing, fuselage, joints and control surfaces. The effectiveness of the sensor relies on the type of sensors used and the suitability of the sensors for long-term operation and conditions [6].

Strain-based sensors, vibration sensors, ultrasonic sensors, acoustic emission sensors and infrared thermography systems are a few widely used technologies. However, no single sensor technology is universally optimal, and each method involves trade-offs in sensitivity, environmental robustness and data interpretation complexity, as illustrated in Fig. 2.

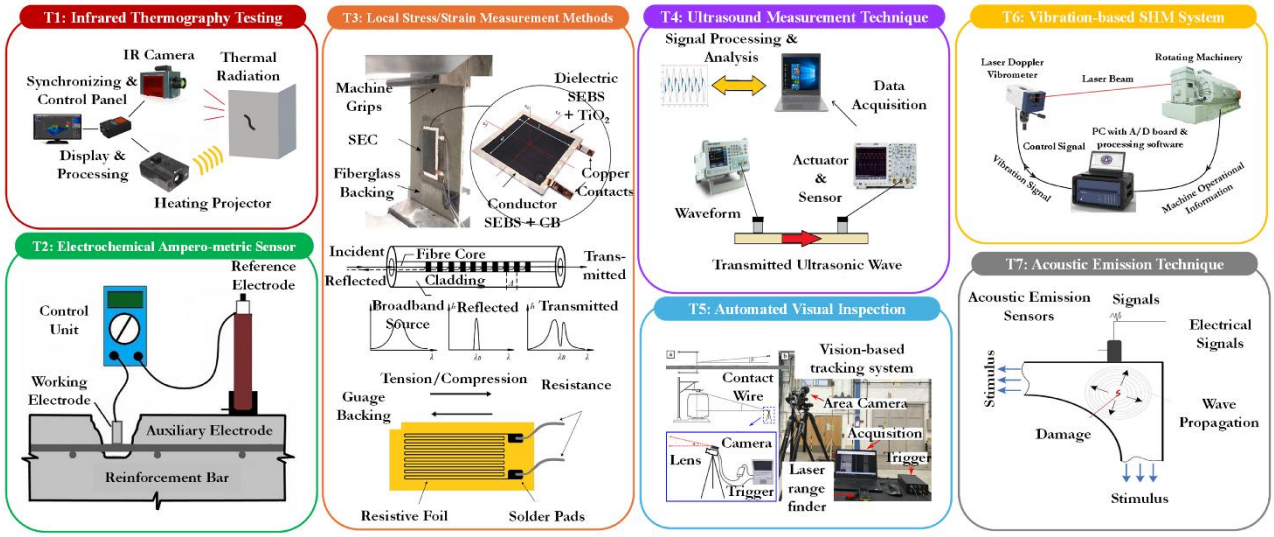

Fig. 2. Overview of commonly used sensing techniques in SHM [8]

Electrical strain gauges, piezoelectric sensors, and fiber-optic sensors are the main structural sensing families. They help in local strain sensing, global vibration monitoring of the structure and detecting distributed damage. Each of these technologies is briefly reviewed below, with electrical strain gauges discussed in further detail in Section 1.3, given their direct relevance to this project.

a. Piezoelectric sensors

The piezoelectric effect is where mechanical strain generates an electrical charge within the material [9]. Piezoelectric sensors work on the above-mentioned operating principle commonly deployed as PZT (lead zirconate titanate) patches or wafers. They have the ability to perform as both actuators and sensors, which enables them to detect structural response while generating mechanical waves within the structure [7]. This dual capability allows them to play a pivotal role in guided wave and

vibration-based health monitoring techniques where mechanical waves are propagated through a structure to detect possible defects [2].

Fig. 3. Piezoelectric disc sensor used for vibration-based SHM applications [9]

A typical example of a piezoelectric disc sensor used in vibration-based structural health monitoring is shown in Fig. 3. These sensors are widely used for detecting impacts and structural damage, especially in composite materials and aircraft panels with respect to aerospace engineering applications. They are also implemented in pipelines, rotating blades and other load-bearing components [7]. The main advantage of a piezoelectric sensor is high sensitivity and the ability to respond over a wide frequency range, which makes them very effective for damage detection methods [9,11]. However, environmental factors such as temperature fluctuations, humidity and mechanical degradation could affect the performance over a large time span [1,2].

b. Fiber-optic sensors (FOS)

Fiber-optic sensors detect structural changes by measuring the variations in the properties of light transmitted through optical fibers. The characteristics of the sensor, such as light intensity, phase, wavelength within the fiber can be altered with changes in strain, temperature, vibration and even structural deformation. Precise measurements of structural conditions and damage can be detected by monitoring these changes [1,9].

Several types of fiber optic sensing technologies have been developed for SHM. A Fibre Bragg Grating (FBG) sensor measures strain or temperature via shifts in the reflected light wavelength, and it is the most widely used type [9]. Fiber-optic sensors offer several advantages. They are lightweight and immune to electromagnetic interference. They are also quite durable in harsh environments [4].

With the advancements in technology, structural sensors have evolved from mere measurement tools to monitoring systems that support reliability, safety and efficiency in aviation. However, the strain gauge remains one of the most widely adopted and significant approaches for load monitoring and fatigue assessment in aviation.

1.3. Strain gauge sensors

Among the sensing technologies introduced in the previous section, strain gauges are the most widely adopted for structural monitoring in aviation. They are directly bonded to critical load-bearing structures such as wings, fuselage panels, and landing gears to measure localised structural deformation under operational loading conditions, as shown in Fig. 4.

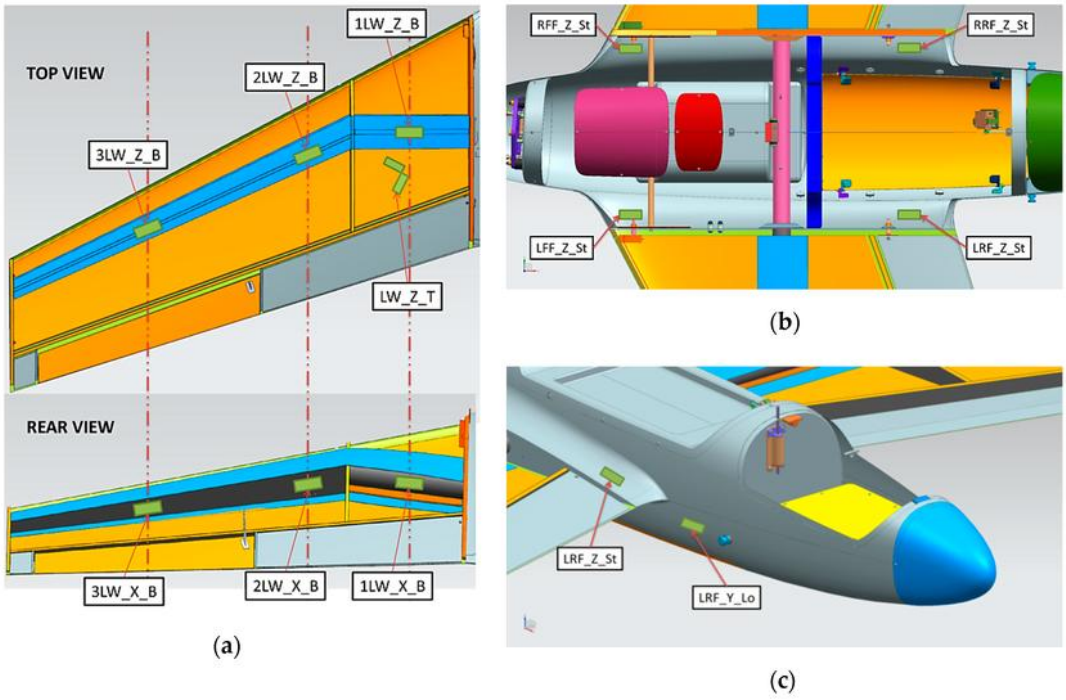

Fig. 4. Strain gauges location (a) on the wing, (b) on the top fuselage and (c) side fuselage [11]

They are particularly useful for monitoring structural strain and fatigue accumulation under operational loading. By tracking resistance changes in the gauge element, fatigue accumulation can be detected before it leads to structural damage. The sensitivity of a strain gauge to deformation is characterised by its gauge factor, which directly relates the measured resistance change to the applied strain.

1.3.1. Working principle of strain gauges

A strain gauge comprises a thin metallic foil or a 3D printed conductive grid, which is bonded to or attached to the surface of the structural component. When the structure is subjected to mechanical loading, the strain is transferred to the gauge element. As illustrated in Fig. 5, the applied strain changes the geometry of the conductive path, thereby varying the electrical resistance. This change in resistance forms the basis for strain measurement [13,14].

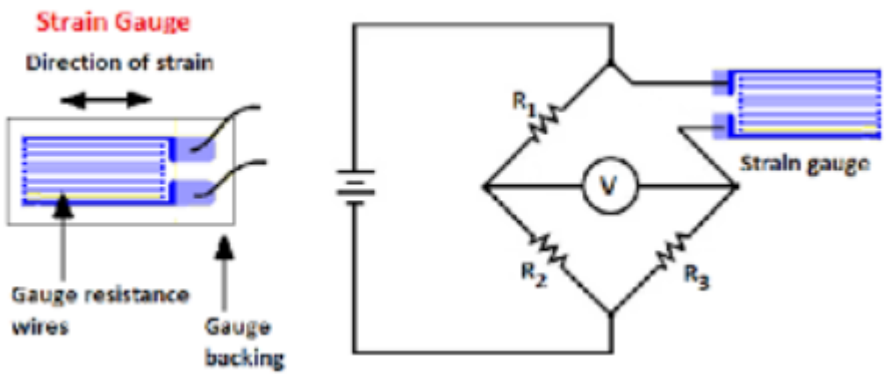

Fig. 5. Diagram of the Working Principle of the Strain Gauge [12]

The electrical resistance of a conductor is determined by:

$$R = \rho \frac{L}{A} \tag{1.1}$$

where R is the electrical resistance, ρ is the electrical resistivity of the material, L is the length of the conductor, and A is its cross-sectional area [13].

When the structure undergoes axial strain ϵ, the length and cross-section of the gauge change. For small deformations, the relative change in resistance can be approximated as [14]:

$$\frac{\Delta R}{R} = \frac{\Delta \rho}{\rho} + \frac{\Delta L}{L} - \frac{\Delta A}{A} \tag{1.2}$$

The terms associated with changes in length and cross-section represent geometric effects related to Poisson's ratio, while the resistivity term represents the piezoresistive effect.

In practical aircraft monitoring systems, strain gauges are commonly connected in Wheatstone bridge configurations such as quarter-bridge, half-bridge, or full-bridge arrangements. These bridge circuits convert very small resistance changes into measurable voltage signals while also improving temperature compensation and measurement sensitivity [12].

In practical scenarios in aircraft monitoring systems, the strain gauges are connected in Wheatstone bridge configurations like the quarter bridge, half bridge or the full bridge configurations. These bridge converts small resistance changes into voltage signals [15].

1.3.2. Gauge factor and sensitivity

Gauge factor (GF) is a measure of the sensitivity of a strain gauge, which is expressed as the ratio between resistance change and applied mechanical strain [13].

$$GF = \frac{\Delta R/R}{\epsilon} \tag{1.3}$$

where ϵ represents the mechanical strain applied to the gauge. Metallic foil strain gauges commonly used in aerospace applications have an approximate value of 2.0 [12,13]. In contrast, printed or composite sensors based on strain gauges exhibit lower and tunable gauge factors strongly depending on the material composition and processing conditions.

Improvement of the sensitivity of strain gauges has been a burning topic of research. There are various approaches to it. One approach is to use semiconductor materials or CNT-based composites, which have higher intrinsic gauge factors. The second approach is to integrate it in a Wheatstone bridge layout. This approach increases the output signal amplitude, effectively improving the measurement resolution. The measured resistance can be converted into strain once the gauge factor is determined using [5,12]:

$$\epsilon = \frac{1}{GF} \frac{\Delta R}{R} \tag{1.4}$$

This relationship allows for monitoring live strain measurement during flight and converting it into structural load histories.

1.4. Wheatstone bridge for strain measurement

A Wheatstone bridge is predominantly used to convert the extremely small resistance change in a strain gauge into a measurable voltage signal. In this layout, the circuit consists of four resistive arms, excitation voltage V_s is applied across one end, and the output voltage V_o is measured on the other. In the balanced condition, the resistance ratio of one branch must be equal to that of the other branch, resulting in a null output voltage. So when strain is applied, the resistance of the gauges changes by a small amount ΔR, interrupting the balance of the bridge and producing a differential output proportional to the strain [17,18].

$$\frac{R_1}{R_2} = \frac{R_3}{R_4} \Rightarrow V_o = 0 \tag{1.5}$$

Different Wheatstone bridge configurations are used depending on the required sensitivity and needed compensation characteristics.

1.4.1. Quarter-bridge configuration

In a quarter-bridge layout, only one of the four resistive arms acts as an active strain gauge, while the remaining three are fixed resistors. Fig. 6 shows how a change in resistance of the active gauge disturbs the bridge balance, producing a measurable output voltage [18].

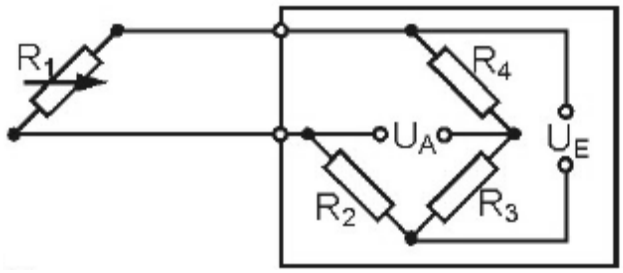

Fig. 6. Quarter Bridge Configuration [16]

For small resistance changes (| ΔR |≪ R), the output voltage is approximately:

$$V_o = \frac{1}{4}\frac{\Delta R}{R} V_s \tag{1.6}$$

Substituting the strain gauge relation gives:

$$V_o = \frac{1}{4} GF\, \varepsilon\, V_s \tag{1.7}$$

This configuration is commonly implemented in basic strain measurements as it is quite simple. However, its sensitivity is relatively lower and limits temperature compensation [8].

1.4.2. Half-bridge configuration

In a half-bridge layout, two of the resistive arms act as active strain gauges. These are typically arranged such that one experiences tensile strain while the other undergoes compressive strain, producing opposite resistance changes. As illustrated in Fig. 7, this arrangement causes a greater imbalance in the Wheatstone bridge compared to the quarter-bridge configuration, resulting in a higher output voltage [17]. This configuration, therefore, improves sensitivity and also provides partial compensation for temperature effects.

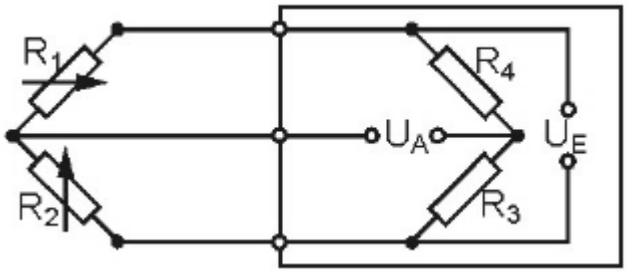

Fig. 7. Half-Bridge Configuration [16]

The approximate bridge output for small resistance changes is:

$$V_o = \frac{1}{2}\frac{\Delta R}{R} V_s \tag{1.8}$$

or

$$V_o = \frac{1}{2} GF\, \varepsilon\, V_s \tag{1.9}$$

When compared to the quarter bridge configuration, the sensitivity is doubled, and temperature-induced variations tend to cancel out more effectively [18].

1.4.3. Full bridge (4 active gauges)

In a full-bridge configuration, all four resistive arms are active strain gauges. Fig. 10 depicts the arrangement in which two gauges experience tensile strain while the other two undergo compressive or transverse strain, maximising the output signal. This configuration provides the highest sensitivity and offers effective compensation for temperature and environmental effects.

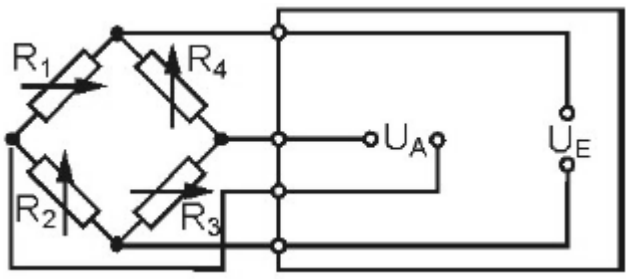

Fig. 8. Full-bridge Configuration [16]

Similar to the half bridge configuration, in an axial setup, the gauges are often aligned in a way that two gauges experience tensile strain, while the other, which measures the transverse or compressive strain [1]:

$$\varepsilon_t = -\nu\varepsilon_l \tag{1.10}$$

where ν is Poisson's ratio and ε_l is the longitudinal strain.

For this configuration, the bridge output can be approximated as:

$$V_o = GF(1+\nu)\varepsilon_l V_s \tag{1.11}$$

In the ideal case where the gauges experience equal and opposite strain effects, the bridge output can be simplified to:

$$V_o = GF\,\varepsilon\,V_s \tag{1.12}$$

This configuration provides maximum sensitivity and excellent temperature compensation because identical temperature effects occur in all four arms and largely cancel out.

Practically, the output voltage from a Wheatstone bridge is very small, often in the millivolt range. Therefore, to amplify the signal before processing, instrumentation amplifiers are used. Overall, because of their high sensitivity, the bridges are adopted and implemented widely in precision strain measurement and SHM applications [2,17].

1.5. Additive manufacturing of strain sensors

Recent advancements in additive manufacturing have enabled the direct fabrication of strain-sensing elements integrated within structural components. Unlike conventional bonded foil gauges, these sensors rely on printed conductive paths and offer significant design flexibility.

Several studies have investigated the design, fabrication, and characterisation of 3D-printed strain sensors using conductive polymer filaments, each adopting different structural geometries, substrate materials, and testing conditions. Reviewing these works provides important context for understanding the design choices, performance trade-offs, and known limitations of sensors of the type employed in this project.

1.5.1. Sensor design strategies

Based on existing research, 3D-printed strain sensors can be broadly classified into two main configurations:

- Surface-mounted printed sensors, where conductive tracks are deposited on a substrate, similar to traditional foil gauges
- Embedded sensors, where conductive pathways are integrated within the structure during fabrication

In one research, [14], a comparable approach based on an FDM-printed strain gauge using Proto-Pasta conductive PLA deposited onto a non-conductive PLA substrate was presented. The main components of the printed strain gauge are identified in Fig. 9, including the carrier material, conductive grid, and contact pads, where the grid functions as the sensing element. The sensor was

fabricated on a Prusa i3 MK3 printer using a 0.4 mm nozzle, with the conductive traces embedded into the PLA base to improve inter-layer adhesion, which is a known challenge in multi-material FDM printing.

The authors reported a near-linear relationship between applied strain and measured resistance, validated using an Instron E10000 tensile testing machine. However, a 6.05% increase in residual resistance was observed between the start and end of each loading cycle, attributed to the viscoelastic behaviour of PLA and restructuring of the carbon black percolation network.

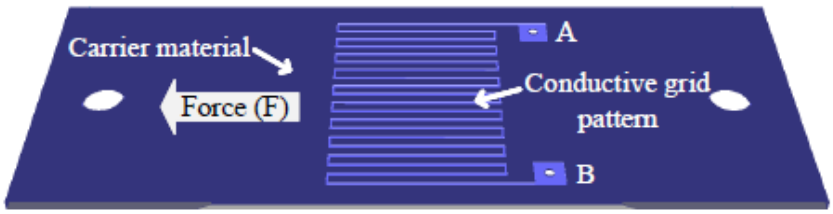

Fig. 9. Components of the FDM-printed strain gauge showing carrier material, conductive grid pattern, and contact pads [13]

A lagging of the resistance response relative to applied strain was also identified. These findings highlight a fundamental limitation of carbon-black-filled PLA sensors: while suitable for slow or quasi-static strain monitoring, such as long-term creep, they are less well suited to dynamic or rapidly varying load conditions. Importantly, the study also demonstrated that incorporating conductive PLA traces reduced the ultimate tensile strength of specimens by approximately 73% compared to non-conductive PLA, raising important considerations for sensor placement and structural integration [13].

A more refined design was undertaken in another study [19] where a two-layer 3D-printed strain gauge was fabricated, consisting of a meander-shaped measuring grid of conductive PLA (Protopasta Conductive PLA) printed on a non-conductive PLA substrate, closely mirroring the layout of a conventional metal foil gauge. Fig. 10 provides a detailed view of the sensor structure, including the PLA substrate, conductive grid pattern, and bonding to a steel plate, which enables strain transfer. The printed sensor was bonded to a stainless steel plate using a cold-curing superglue and subjected to a bending load of 30 N, with gauge placement determined through prior finite element analysis in COMSOL Multiphysics to identify the region of maximum strain. Results demonstrated a nearly linear resistance response with a correlation coefficient R^2 of 0.996 and a linearity error within ±4%.

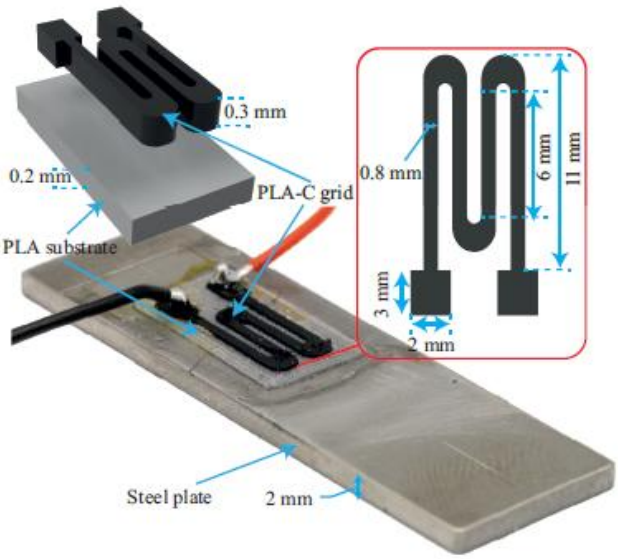

Fig. 10. Structure of the 3D-printed strain gauge showing the PLA substrate, conductive PLA measuring grid, and bonding onto a steel plate acting as the load-bearing element [19]

The gauge factor was calculated to be 8.3, approximately four times higher than that of a conventional metal foil gauge. However, polymer-induced creep was observed as a superimposed drift in resistance during sustained loading, attributed to reorganisation of the conductive particle network within the filament. The study confirms that 3D-printed sensors of this type can be bonded to metallic structural elements and exhibit useful sensitivity, but that the creep behaviour of the conductive polymer remains a key challenge [19].

A recent study [20] extended the application of FDM-printed sensors to the marine industry, fabricating a two-layer device comprising a CNT-enriched PLA sensing element printed on an Acrylonitrile Styrene Acrylate (ASA) substrate using an Ultimaker S3 printer. Fig. 1(a) outlines the sensing geometry, while Fig. 1(b) presents the fabricated device, including the substrate, sensing element, and contact pads. The sensing element geometry was a simple rectangular piezoresistor measuring 50 mm × 4 mm, with integrated contact pads that could be connected directly to readout circuitry via standard soldering, eliminating the need for wire bonding. A notable feature of this work was the investigation of post-printing thermal sintering as a means of improving sensor performance. Annealing at 102 °C for up to 20 hours produced a total resistance reduction of 44%, improved gauge factor from 0.54 (unsintered) to 0.95 (sintered 20 h), and significantly reduced hysteresis and resistance variability. The correlation between sintering time and linearity was found to be strongly negative (Pearson coefficient −0.99), indicating that longer annealing produces more consistent and repeatable sensor behaviour. The authors attributed these improvements to a transition of the PLA microstructure from an amorphous to a semi-crystalline state, which stabilises the CNT conductive network. The study also examined sensor response under alternating hogging and sagging bending modes, observing a nonmonotonic resistance-strain behaviour consistent with competition between formation and destruction of CNT percolation pathways — a phenomenon also reported elsewhere in the literature for CNT/polymer composites.

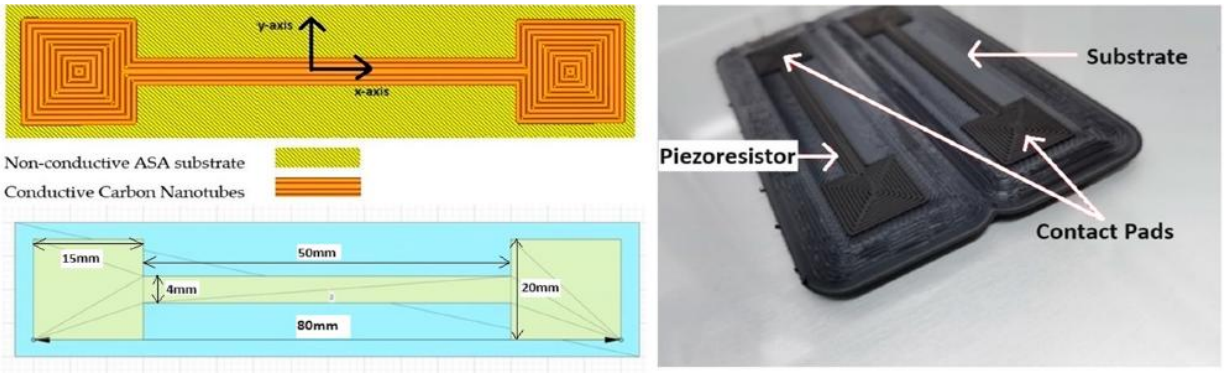

Fig. 11. Geometry of the 3D-printed strain gauge showing the conductive sensing grid and contact pads [20]

These findings are particularly relevant to structural applications, as they suggest that post-fabrication thermal treatment can meaningfully improve sensor linearity and repeatability without high additional cost.

A structurally different approach was taken [15], where both FDM and stereolithography (SLA) techniques were used to fabricate the structural body of micro force sensors, onto which conventional commercial foil strain gauges (Omega SGD-1.5/120-LY13, 120 Ω) were manually bonded. As shown in Fig. 12, two sensor geometries were developed: a parallel-beam load cell printed in PLA using an FDM printer, and a cantilever beam sensor printed in HTM 140 resin using an SLA printer. Finite element analysis was used to optimise the structural design and identify locations of maximum strain for gauge placement. The load cell achieved a force resolution of 56 µN with a sensitivity of 6.845 V/N and a linearity of 1.14%. In comparison, the cantilever beam sensor achieved a resolution of 4.3 µN at a sensitivity of 525.15 V/N.

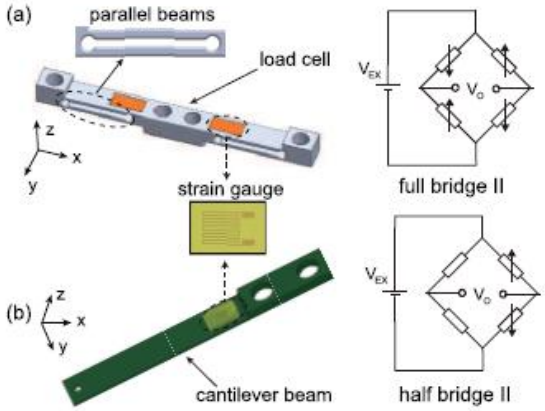

Fig. 12. Design schematics (left) and corresponding Wheatstone bridge circuits (right) for (a) parallel-beam load cell sensor and (b) cantilever beam sensor [15]

Both configurations used Wheatstone bridge circuits, a full bridge for the load cell and a half bridge for the cantilever, with instrumentation amplifiers to condition the sub-millivolt output signals. Although this work differs from the all-printed approach in that the sensing element is not itself 3D-printed, it demonstrates that 3D-printed polymer structures can serve as effective flexure elements for strain-based force sensing and highlights the importance of FEA-guided design and bridge configuration selection in achieving high measurement resolution.

1.6. Conductive materials for 3D-printed sensors

The performance of sensors manufactured through additive manufacturing highly depends on the conductive material used in the fabrication. Commonly, a combination of thermoplastic polymers with conductive fillers is employed as they exhibit piezoresistive behaviour.

Fig. 13. Types of conductive filaments (a) Carbon-filled [21] (b) Metal-filled (Copper) [22]

As illustrated in Fig. 13, these materials are typically available as carbon-filled filaments or metal-filled filaments, each offering different electrical and mechanical properties. Electrical conduction occurs through a percolation network formed by these fillers within the polymer matrix.

1.6.1. Types of conductive filaments

Conductive filaments used in 3D printed sensors can be broadly categorised into three material families: carbon-based, metal-filled, and ionic or liquid-based systems.

Carbon-black-filled polymers, such as Protopasta Conductive PLA, are the most widely used for piezoresistive strain sensing applications. These materials mix a standard polymer matrix such as PLA or TPU with conductive carbon black particles, achieving printed resistivities in the range of 30–115 Ω·cm depending on print orientation and parameters [13,14]. Carbon nanotube-enriched composites represent a more advanced variant, offering tunable gauge factor and improved linearity through thermal treatment [18], though they are less commercially accessible than carbon-black alternatives.

Metal-filled filaments incorporate metallic powders such as silver, copper, or bronze dispersed within a polymer matrix. While they offer higher conductivity than carbon-based systems, the discontinuous nature of the metal particle network means conductivity remains significantly below that of bulk metals. A related approach involves post-processing carbon-filled printed electrodes through electrodeposition of metallic coatings such as gold nanoparticles, enabling noble-metal surfaces suitable for electrochemical sensing [21].

Liquid metal and conductive ink systems represent a third category, primarily used in flexible and stretchable sensing applications. Liquid metals such as gallium alloys contained within microchannels maintain high conductivity under large deformations, while conductive inks deposited through screen or inkjet printing enable hybrid fabrication approaches on 3D printed substrates [21]. However, these systems are less suited to rigid structural sensing applications and were not considered further in this project.

1.7. Temperature effects on resistance-based sensors

Resistance-based sensors (strain gauges, conductive-PLA sensors, RTDs, concrete resistivity probes, etc.) are highly sensitive to temperature. Temperature affects both the sensor element and the measurand (e.g., structure, concrete pore fluid), and several error sources appear in practice. A few ways in which temperature affects resistance-based sensors:

a. Intrinsic temperature coefficient of resistance (TCR)

The inherent nature of the resistance-based sensors makes them sensitive to temperature by default; this phenomenon is described by the temperature coefficient of resistance (TCR).

In metallic sensing elements, such as platinum resistance temperature detectors (RTDs), resistance typically increases approximately linearly with temperature [25]. For strain-type sensors, the general relation between resistance, strain, and temperature includes a TCR term, so the mean resistance level shifts with temperature, independent of strain [24]. In piezoresistive 3D printed conductive PLA sensors, theory explicitly separates strain-dependent terms from the temperature term, which only affects the mean resistance and must be compensated if temperature varies significantly [24]. The temperature dependence of resistance is evident in Fig. 14, where resistance increases with temperature, indicating a positive temperature coefficient.

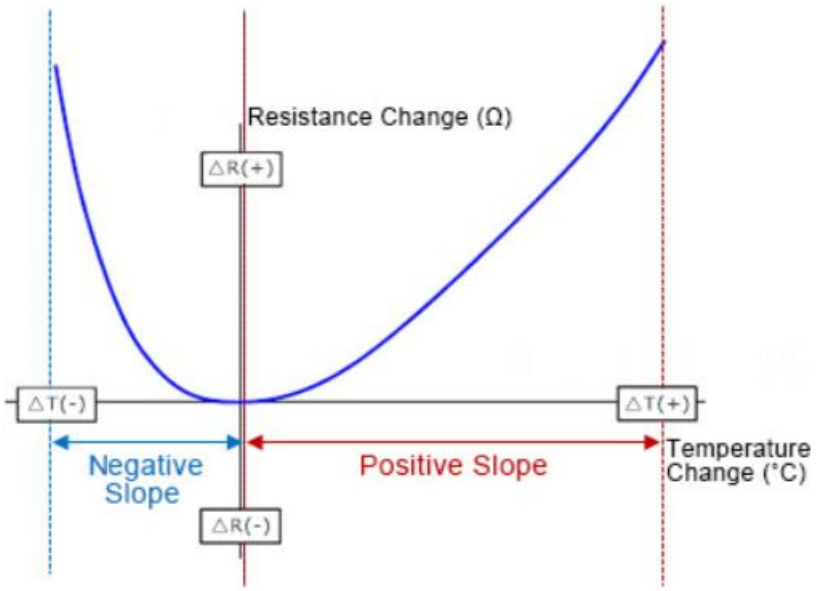

Fig. 14. Relationship between ΔR and ΔT for a temperature-sensitive component

The horizontal axis represents the temperature change (ΔT), while the vertical axis represents the change in resistance (ΔR). At the reference temperature (ΔT = 0), the resistance change is zero. When the temperature increases, the resistance increases with a positive slope, indicating a positive temperature coefficient. When the temperature decreases, the resistance decreases with a negative slope. The curved (nonlinear) shape of the graph shows the variation in resistance.

b. Thermo-mechanical effects (CTE mismatch)

Temperature variations can also influence sensor measurements through thermo-mechanical effects. When the sensor material and the host structure have different coefficients of thermal expansion

(CTE), temperature changes can produce apparent strain in the sensing element even if no mechanical loading is present [14]. This occurs because the sensor and the substrate expand or contract by different amounts. For bonded sensors (foil gauges, embedded conductive tracks, FBG strain sensors), this can be a major error source unless materials with similar CTEs are chosen or appropriate compensation is used [8,21].

c. Temperature-dependent material or medium properties

In some sensing applications, temperature affects not only the sensor itself but also the properties of the surrounding material or medium being monitored. For example, in resistivity-based sensors used to measure moisture content in concrete, electrical resistivity is strongly influenced by both temperature and water saturation.

Experimental studies have shown that within temperature ranges of approximately 0–40 °C, resistivity in concrete can change by roughly 3–5 % per degree Celsius, and may decrease by about half when the temperature increases by around 20 °C [25]. Measurements from embedded resistivity sensors have demonstrated that the relationship between temperature and resistivity often follows Arrhenius-type behaviour. As a result, temperature corrections are required to obtain reliable estimates of material properties such as water content or conductivity [24].

To reduce the influence of temperature on resistance-based sensors, several compensation strategies can be applied. Temperature measurement and correction is the most common approach, where the sensor output is adjusted using known temperature–resistance relationships such as TCR-based corrections. Material selection also plays an important role; choosing sensing materials with low temperature sensitivity or matching the coefficient of thermal expansion (CTE) between the sensor and the host structure helps minimise thermally induced resistance changes. In addition, sensor configuration techniques, such as differential measurement arrangements, can help cancel common temperature effects between sensing elements. Finally, proper calibration across the expected temperature range and careful experimental design, including shielding from environmental fluctuations, can significantly improve measurement reliability by separating temperature effects from actual strain signals.

2. Sensor Development and Characterisation

To develop a functional 3D printed strain sensor, material selection, geometry of the sensor, and the fabrication process must be taken into close consideration. The first step is to identify a suitable conductive filament for fabrication, determine the temperature coefficient and propose a possible way to compensate. Furthermore, electrical integration methods are also investigated, along with determining reliable methods for data acquisition. The chapter concludes with an evaluation of the sensor's sensitivity to temperature variations, assessing potential drift effects under real operating conditions.

2.1. Material selection

The choice of conductive filament material is critical to the performance of a 3D printed piezoresistive sensor, as it directly determines the electrical resistance, gauge factor, and mechanical compatibility of the sensing element. The selection process involved comparing materials, printed electrical resistance and practical printability, to identify the most suitable material for strain sensing in a rigid structural application

2.1.1. Initial comparison

From the wide array of commercially available filaments, two were selected and further evaluated:

- Conduction PLA filament of Protopasta – It is a semi-flexible material, composed of PLA, a dispersant and conductive carbon.
- Filaflex conductive – It is a flexible TPU elastic filament, an easy-to-print material. After stretching, it returns to its original shape, without deforming or breaking, presenting excellent mechanical properties.

Table 2. Properties of the proposed filaments [26,27]

Property	**Filaflex Conductive (TPU)**	**Protopasta Conductive PLA**
Manufacturer	Recreus (Spain)	Protopasta (USA)
Base polymer	TPU (Thermoplastic Polyurethane)	PLA (Polylactic Acid)
Elongation at break	~100%	Low (fracture under repeated bending)
Density	1.35 g/cm^3	1.24 g/cm^3
Elastic recovery	Excellent (returns to original shape)	Limited
Recommended current	Low current only	Low voltage / low current
Volumetric resistivity (bulk)	~3.9 Ω·cm	~15 Ω·cm (unprinted filament)
Volumetric resistivity (printed)	Strongly process-dependent	30 Ω·cm (in-plane), 115 Ω·cm (Z-axis)
Sensitivity to extrusion deformation	Very high	Moderate

Both materials have comparable bulk resistivity; however, their post-printing electrical behaviour, mechanical response, and suitability in sensing applications might differ and must be evaluated in detail.

2.1.2. Baseline electrical resistance of unprocessed conductive filaments

Resistance measurements were performed on unprocessed filament samples to understand the intrinsic electrical property before printing to establish a baseline. This test aimed to verify the

relationship between the electrical resistance and the length of the filament. Filaments of length 200 mm and 500 mm were assessed by placing a digital multimeter directly at the free ends. The measurements were repeated twice to reduce uncertainty and improve repeatability.

Table 3. End-to end resistance readings of unprocessed filaments

Filament	Length (m)	Resistance (K Ω)
Protopasta	200	6.85
	500	16.265
Filafex	200	6.445
	500	16.115

From the obtained results, as seen in Table 3, the resistance increases linearly with the length of the filament, following the electrical theory, $R \propto l$.

2.1.3. Single extrusion resistance characterisation

To assess the influence of the FDM process on the electrical behaviour of conductive filaments, single-extrusion specimens were printed and analysed. This approach isolates the conductive path and allows evaluation of how printing affects resistance compared to the raw filament, while also enabling repeatability assessment.

Single extrusions with dimensions 200 mm × 0.4 mm × 0.2 mm were fabricated. To improve measurement reliability and evaluate repeatability, five identical extrusions were printed and arranged as parallel conductive tracks within the same specimen.

The key printing parameters used for the single-extrusion specimens are as follows:

- Nozzle diameter: 0.4 mm
- Layer height: 0.2 mm
- Infill: 100% (solid extrusion)
- Extrusion width: 0.4 mm

Both the conductive filaments were printed and tested using this procedure. Protopasta specimens were printed at a nozzle temperature of 225 °C, while Filaflex specimens were printed at 230 °C as per the manufacturer‘s suggestion [28]. After printing, all samples were allowed to cool to room temperature before resistance measurements were performed. Electrical resistance measurements were then performed using a digital multimeter by measuring the end-to-end resistance of each printed extrusion.

The Protopasta conductive PLA extrusions exhibited resistance values in the range of approximately 387– 408 kΩ, with an average resistance of 393.6 kΩ.

In contrast, the Filaflex conductive TPU extrusions showed significantly higher resistance values, in the range of approximately 0.83–0.93 MΩ, with an average resistance of 0.88 MΩ. Although the Filaflex samples also demonstrated reasonable repeatability, the substantially higher resistance suggests reduced electrical conductivity after printing.

2.1.4. Simplified sensor print (pad-to-pad measurement)

To characterise the behaviour of the conductive filament within an integrated sensing geometry, a test gauge was designed and fabricated. The sensor consisted of a serpentine conductive track deposited on a non-conductive PLA substrate to replicate the geometry of a strain-sensing element while enabling controlled electrical measurements.

The substrate dimensions were 10 mm × 45 mm, with a conductive track width of 0.4 mm and a thickness of 0.2 mm. The serpentine layout increased the effective conductive path length, allowing measurable resistance changes within a compact geometry.

The sensor was manufactured using a multi-material FDM process. A PLA base layer was printed first, followed by a manual filament change to deposit the conductive material. The simplified sensor geometry is defined in Fig. 15, showing the serpentine conductive track and contact pads used for pad-to-pad resistance measurements.

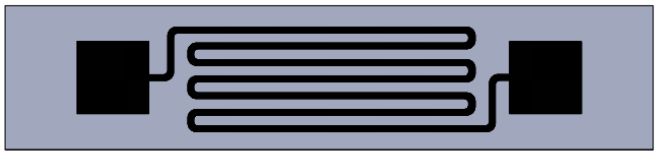

Fig. 15. CAD model of the simplified strain gauge (10 mm × 45 mm substrate, 0.4 mm track width).

The primary objective at this stage was to evaluate the printability, electrical behaviour, and adhesion between the conductive filament and the base material; therefore, the full geometry was not required for the present investigation.

During the slicing process, the toolpath and material transition for the conductive track were defined, as shown in Fig. 16, where the simplified strain gauge geometry is prepared for multi-material printing in PrusaSlicer. At this point, the PLA filament was unloaded and replaced with the selected conductive filament, after which sufficient purging was performed to ensure complete removal of the base material from the nozzle before printing the conductive paths, and then the print was resumed to deposit the conductive strain gauge geometry directly onto the PLA base.

The main manufacturing parameters are summarised below:

- Base material: Standard PLA (non-conductive)
- Nozzle temperature for Protopasta TPU: 225°C
- Nozzle temperature for Filaflex: 230°C
- Heated bed temperature: 60 °C
- Layer height: 0.2 mm
- Number of perimeters (shells): 2

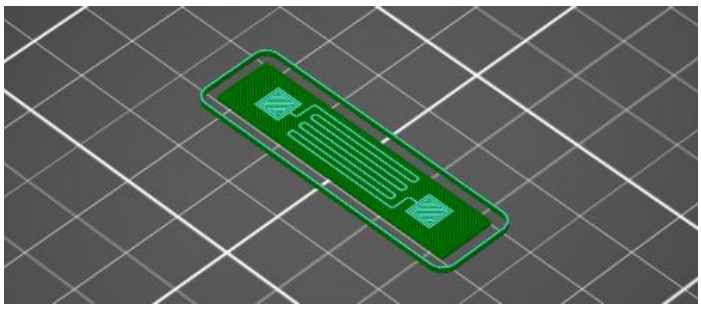

Fig. 16. Simplified strain gauge - sliced model in PrusaSlicer

Once the specimens cooled down to room temperature, measurements were performed in a pad-to-pad configuration using a digital multimeter.

Table 4. Pad-to-pad resistance measurements of a fully printed (simplified) sensor

Conductive Filament	**Measurement Location**	**Resistance**
Filaflex Conductive TPU	Centre pads	1.097 MΩ
Protopasta Conductive PLA	Centre pads	275.03 kΩ

Resistance measurements were conducted using the setup in Fig. 17, where (a) corresponds to TPU and (b) to conductive PLA, highlighting the difference in measured resistance values. The sensor printed using Filaflex Conductive TPU exhibited resistance values in the megaohm range, indicating relatively low electrical conductivity in the integrated sensor geometry. While electrical continuity was achieved, the high resistance suggests that the conductive pathways formed during printing were less effective, which may be related to the highly flexible nature of the material and its behaviour during extrusion and cooling.

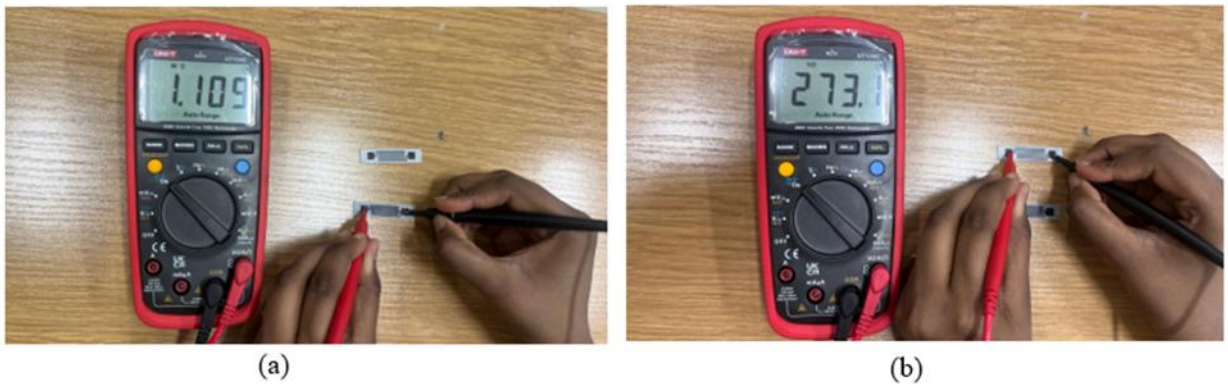

Fig. 17. Experimental setup (a) Filaflex conductive TPU and (b) Protopasta conductive PLA

In contrast, the sensor printed using Protopasta Conductive PLA demonstrated much lower resistance values in the kilo-ohm range. This indicates more stable and continuous conductive paths within the printed strain gauge geometry. The lower resistance is advantageous for strain gauge applications, as it enables improved signal quality and reduced sensitivity to measurement noise. Based on these observations, Protopasta Conductive PLA was identified as the more suitable material for the fabrication of an integrated printed strain gauge sensor in this feasibility study.

2.1.5. Effect of temperature on the electrical resistance of the simplified sensor

An additional experiment was conducted to investigate the effect of temperature on the electrical resistance of the printed strain gauge (simplified) sensor fabricated using Protopasta Conductive PLA.

After printing, the sensor specimen was allowed to stabilise at room temperature (approximately 20 °C). The heated build plate of the 3D printer was then used as a controlled heat source to increase the temperature of the specimen. The temperature was raised in increments of 5 °C, from 20 °C up to 60 °C. At each temperature step, the specimen was allowed to stabilise for 4 to 5 minutes to ensure thermal homogenisation. The surface temperature of the specimen was cross-checked using a handheld digital infrared thermometer to verify the set build plate temperature. Following this stabilisation period, multiple resistance measurements were taken using a digital multimeter in a pad-to-pad configuration.

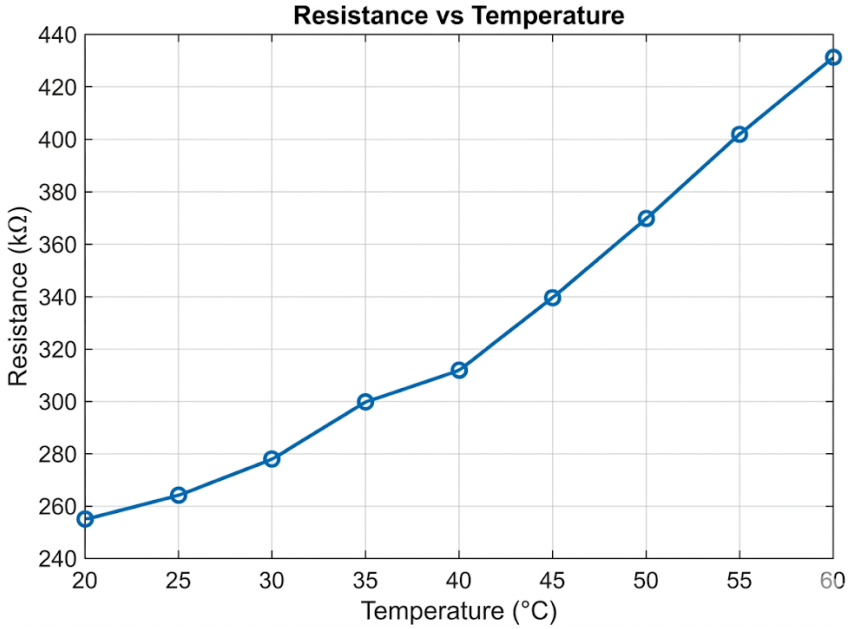

Fig. 18. Resistance and temperature relationship of the simplified strain gauge

The measured resistance variation with temperature is presented in Fig. 18, showing a consistent increase across the tested range. The relatively smooth progression of resistance values across temperature steps and the low variation between repeated measurements indicate good measurement repeatability and stable electrical behaviour during heating.

Overall, the observed increase in resistance with temperature confirms that the printed conductive material exhibits a positive temperature coefficient of resistance within the tested range. This behaviour is consistent with expectations for carbon-filled polymer-based conductive composites and highlights the need for temperature compensation in practical strain-sensing applications.

Following the identification of significant temperature dependence in the resistance-based sensing element, a Wheatstone-bridge-based sensor configuration was developed to improve measurement sensitivity and temperature compensation.

Two sensor layouts were designed using a full Wheatstone bridge configuration, consisting of four active resistive elements of 75 mm each, fabricated from conductive PLA. The design considerations included an identical path length for all four resistive elements, uniform track width and thickness, a symmetric layout to ensure balanced bridge conditions and compact geometry suitable for integration on structural components.

2.2. Development of Wheatstone bridge-based sensor architectures

Following the identification of significant temperature dependence in the simplified strain gauge, a Wheatstone bridge–based configuration was developed to improve measurement stability and sensitivity.

Two sensor layouts were designed, each consisting of a full bridge with four active resistive elements of 75 mm, fabricated using Protopasta conductive PLA. Both configurations were designed with identical path lengths, a uniform track width of approximately 0.4 mm, and symmetric geometry to ensure a balanced bridge condition. Based on single-extrusion measurements, the resistance of a 75 mm conductive path was estimated to be approximately 140 kΩ.

The fabrication process was kept consistent across both layouts to eliminate variability due to printing conditions. This allows performance differences to be attributed solely to the sensor geometry.

2.2.1. Design layout I: longitudinal configuration

The ISO 527 Type B tensile specimen was chosen for the base substrate, which ensures that the strain is measured along the primary loading axis. As seen in Fig.19, the design an longitundinal arrangemnets of the resistive arms and is positioned in the middle of the gauge section, where uniform strain distribution is expected.

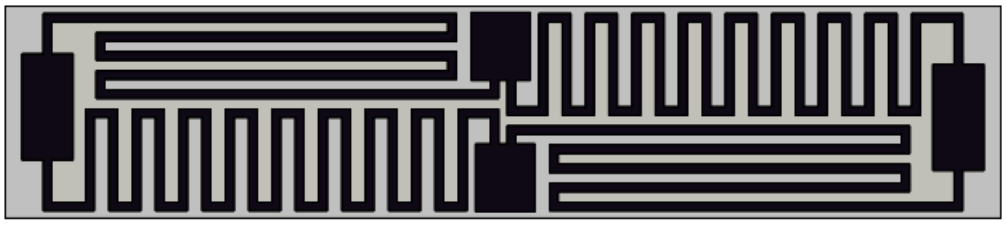

Fig. 19. CAD model of Design Layout I - Longitudinal

The total resistance of the fabricated sensor was measured using a digital multimeter and found to be approximately 137 kΩ, which falls closer to the expected range based on prior resistance predictions.

2.2.2. Design layout II: compact full-bridge configuration

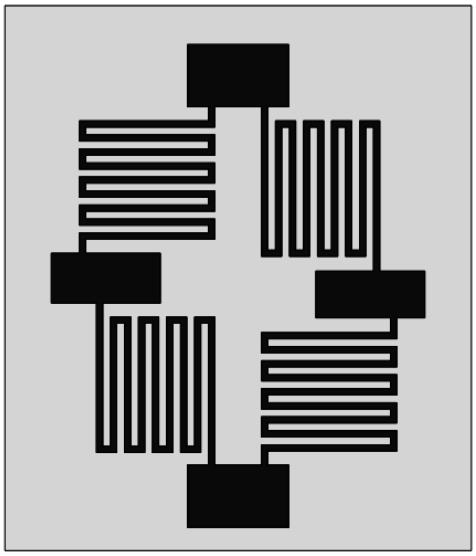

Fig. 20. CAD model of Design Layout II - Compact

The resistance of the compact layout is measured to be 100 kΩ which is much less than the predicted value of 147 kΩ. This could be due to the compact nature of the design as seen in Fig.20, where track overlaps at corners, nozzle deceleration effects, and potential lateral conduction between adjacent tracks collectively reduce the effective resistance below the linear prediction.

2.3. Electrical integration and data acquisition

To measure the sensor's output under mechanical strain, it must be integrated into a circuit. A stable, low-resistance electrical connection between the printed sensor pads and external wiring is needed.

2.3.1. Contact methods

To measure the sensor's output under mechanical strain, it must be integrated into a measurement circuit. A stable, low-resistance electrical connection between the printed sensor pads and external wiring is essential to ensure accurate and repeatable signal acquisition. Poor contact quality introduces variable and unpredictable resistance at the interface, which directly compromises measurement integrity. Furthermore, the data acquisition system must be capable of resolving small voltage changes in the millivolt range, as the bridge output signals produced by piezoresistive sensors under typical structural loading conditions are inherently small. The selection of appropriate connection methods and instrumentation is, therefore, a critical step in developing a reliable sensing system.

a. Copper adhesive tape

In the first approach, a copper adhesive tape was cut into small pieces and applied on the contact pad to which the wire was attached, as shown in Fig. 21. This method was relatively very simple, quick to implement and required no additional thermal processing.

Fig. 21. (a) Copper Adhesive Tape (b) wire attachment using the tape

Experimental observations showed that the measurements yielded from this method were quite unstable and unreliable due to minor movements between the wire and tape. This caused fluctuations and indicated inconsistency.

b. Conductive PLA thermal bonding

In the second approach, the wire was fused with the contact pads using the same conductive filament. As illustrated in Fig.22, a soldering iron was heated to approximately 350 °C and then utilised to facilitate the bonding between the wire and the printed pad on the sensor geometry.

Fig. 22. (a) Soldering pen (b) conductive composite soldered connection

The method was found to be effective as the fused interface between the surface and wire yielded stable and repeatable resistance measurements without introducing additional material.

2.3.2. Instrumentation for Bridge Output Measurement

a. NI 9237 strain/bridge input module

The experimental measurements were conducted using the NI 9237, a dedicated strain and bridge-input module designed for high-accuracy measurement of resistive sensors, as shown in Fig. 23.

The instrument provides built-in signal conditioning, an excitation voltage supply that ranges from 2.5 V to 10 V, and it also allows amplification of low-level signals generated by the resistive sensors.

Fig. 23. NI 9237 Module

The module measures the differential voltage output, which corresponds to the change in resistance due to the induced mechanical strain. This makes the instrument suitable for evaluating the performance of 3D printed strain sensors.

b. NI cDAQ-9173 chassis

The data acquisition system is based on the NI cDAQ-9173 chassis (Fig. 24), which interfaces the measurement module with the host computer.

Fig. 24. NI cDAQ-9173 Chassis

The cDAQ-9173 is a CompactDAQ USB chassis designed to accommodate multiple I/O modules and provide synchronised data acquisition. It acts as the central unit responsible for communication, power distribution, and data transfer.

c. Matlab data acquisition and signal processing

Data acquisition and processing were done using MATLAB, using its capabilities for interfacing with National Instruments hardware. The Analog Input recorder application was used to record the outputs as a dataset. Details like the bridge configuration, resistance, and input voltage were set, and the values were recorded and processed further.

2.4. Temperature drift

Evaluation of temperature drift was conducted for both the layout to assess the stability of the output in the absence of mechanical strain. It is known that temperature changes influence the bridge output, as this directly affects measurement reliability in real-world applications where ambient temperature fluctuations are unavoidable. The objective was to check if the layouts are successful in compensating for the influence of temperature, as seen before in section 2.1.5.

2.4.1. Design layout I

Using the printer bed as the source of heat, the specimen was evaluated from 20°C to 60°C in 5°C increments. A thermometer was placed in contact with the sensor to double-check, as seen in Fig. 25 below.

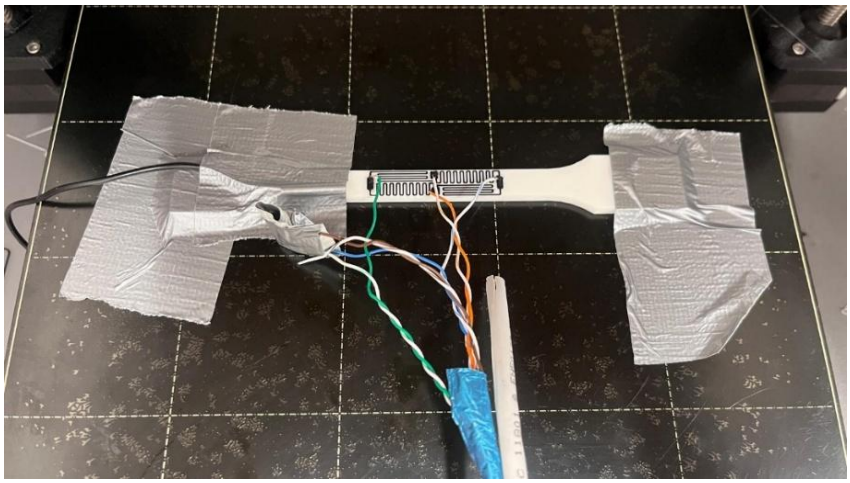

Fig. 25. Experimental Set-up – Specimen I

As depicted in Fig. 26, the sensor output is relatively stable, with minor variations at lower temperatures.

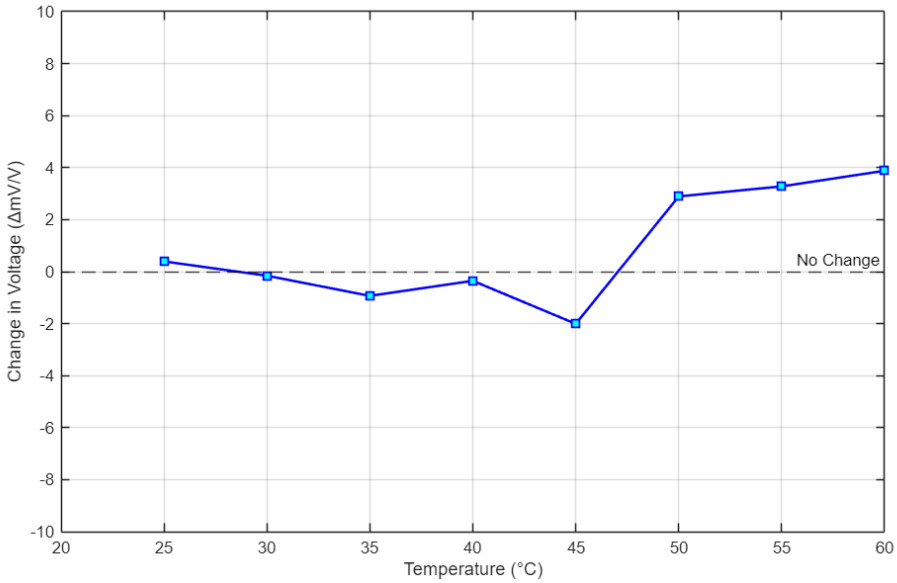

Fig. 26. Change in Output with respect to Temperature – Specimen I

The minor variations at the lower temperature are attributed to the intrinsic property of the conductive material, the non-uniform heating across the specimen and contact resistance. However the are large fluctuations in output voltage beyond 50°C, which is due to the bending of the PLA base material.

Therefore, the observed response at higher temperatures includes both temperature-induced effects and mechanically induced strain, indicating that the printer bed is not suitable for accurate temperature characterisation.

2.4.2. Design layout II

The second layout was evaluated in a different setup to prevent the PLA base from bending. A laboratory oven is used to provide more uniform heating conditions. The specimen was placed on the tray inside the oven, where temperatures were increased from 20°C to 60°C in controlled steps.

A thermocouple was attached to the surface of the sensor to monitor the local temperature, and the readings were cross-checked using a thermal camera.

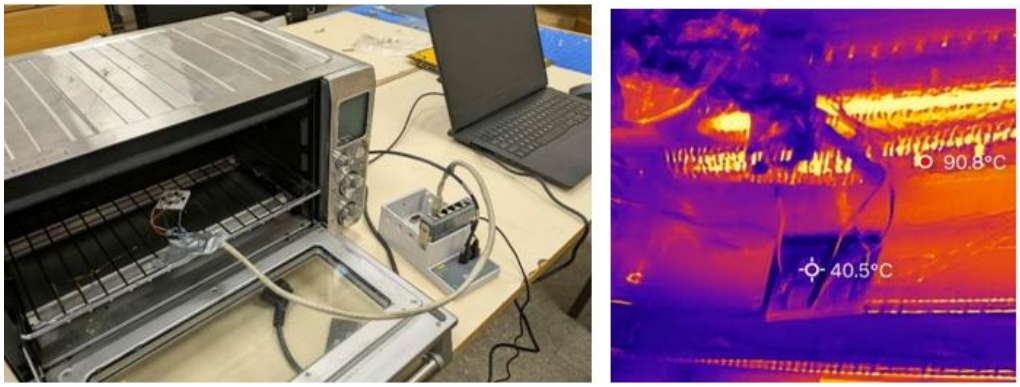

Fig. 27. Experimental Set-up Specimen II

As observed in Figure 28, the step-to-step voltage variation remains close to zero across the entire temperature range, indicating stable sensor behaviour.

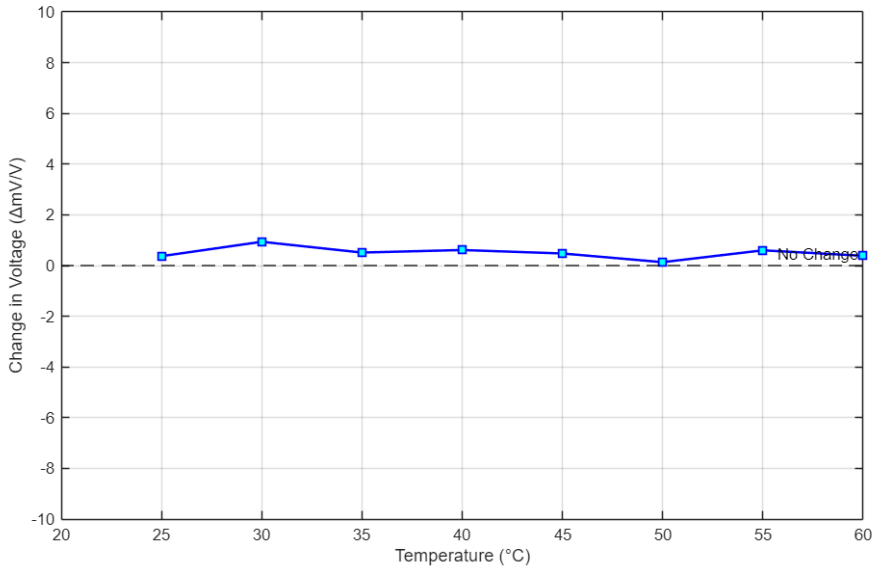

Fig. 28. Change in Output with respect to Temperature – Specimen II

This improved stability is attributed to more uniform and controlled heating in the oven, which minimises temperature gradients and prevents mechanical deformation of the specimen.

2.4.3. Discussion

A direct comparison of the performance of both the sensor layouts under the same range clearly shows the influence of temperature. Design Layout I, tested using a printer bed, exhibited significant variation at higher temperatures due to non-uniform heating and thermo-mechanical deformation of the PLA substratewhile Design Layout II, evaluated in a controlled oven environment, showed minimal step-to-step variation and improved stability across the temperature range.

The improved performance of Design Layout 2 is primarily due to uniform heating conditions, which reduces temperature gradients and prevents structural deformation, and the compact and symmetric geometry of the square layout contributes to a more uniform temperature distribution.

3. Mechanical Testing

The sensor is evaluated under mechanical loading in this section. Two loading condition cases are taken into consideration to assess the performance of the sensor under different strain states.

3.1.1. Tensile testing

To evaluate the strain response and sensitivity under uniaxial loading conditions, tensile testing was performed. The aim is to assess the electrical response with respect to the mechanical load applied.

Fig. 29. (a) Tinius Olsen Universal Testing Machine (b) Experimental Set-Up -Tension

Testing was performed using a Tinius Olsen Universal Testing Machine under controlled loading conditions as seen in Fig 29.

3.1.2. Load determination for tensile testing

The maximum load applied during tensile testing was determined based on the cross-sectional area of the specimen and the allowable stress for PLA.

For Specimen I, the dimensions of the gauge section are:

- Width = 10 mm
- Thickness = 4 mm

The cross-sectional area is:

$$A = 10 \times 4 = 40\ \text{mm}^2 = 4 \times 10^{-5}\ \text{m}^2 \tag{3.1}$$

A maximum stress limit of 10 MPa was selected to ensure that the specimen remains within the elastic region. The corresponding maximum load is:

$$F = \sigma \cdot A = 10 \times 10^6 \times 4 \times 10^{-5} = 400\,\text{N} \tag{3.2}$$

Based on this, tensile testing was conducted from 0 N to 400 N in increments of 80 N.

For Design Layout II, the specimen width was increased to 30 mm, while maintaining the same thickness and material properties. This results in a cross-sectional area three times larger than that of Specimen I. To maintain the same stress level, the applied load was proportionally increased by a factor of three.

$$F_{max} = 3 \times 400 = 1200\,\text{N} \tag{3.3}$$

Accordingly, tensile testing was conducted from 0 N to 1200 N in increments of 240 N.

3.1.3. Tensile analysis - design specimen I

The tensile response of Design Layout I was evaluated by recording the normalised bridge output (V/V) at incremental loading conditions ranging from 0 N to 400 N.

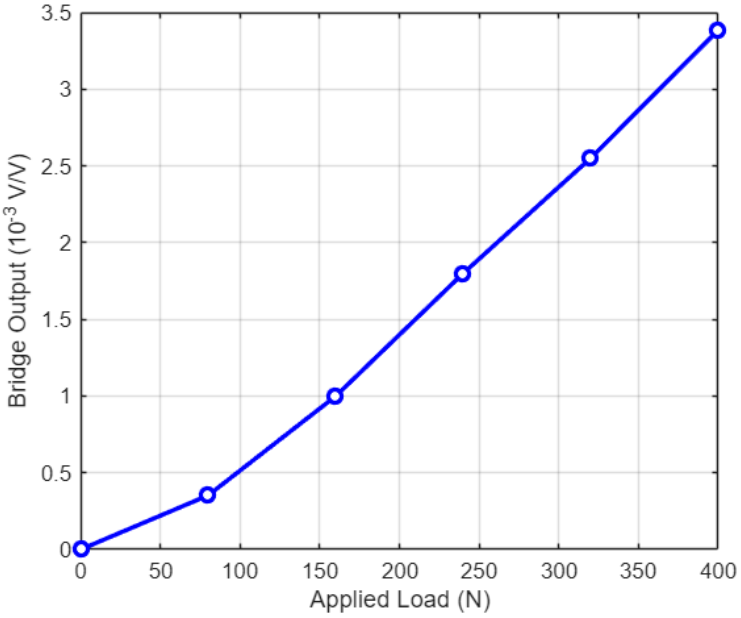

Fig. 30. Bridge output vs. applied load

The output increases consistently with applied load as presented in Fig.30. The slight nonlinearity at low loads is attributed to mechanical seating effects, consistent with behaviour observed in similar additively manufactured sensors.

The strain in the specimen is first derived theoretically using the linear elastic theory. Assuming uniform axial loading, the strain is given by:

$$\epsilon_{th} = \frac{F}{AE} \tag{3.4}$$

where F is the applied load, A is the cross-sectional area, and E is the Young's modulus of PLA. Based on the material datasheet, a modulus of 1146 MPa [28] was used.

This theoretical strain serves as the reference for sensor calibration.

The sensitivity of the strain gauge is measured using the gauge factor (GF), which relates the change in the bridge output to the applied mechanical strain. The gauge factor for a full bridge is defined as:

$$GF = \frac{V_{out}/V_{in}}{\varepsilon} \tag{3.5}$$

To determine this gauge factor experimentally, the normalised bridge output (V/V) was plotted against the corresponding theoretical strain values obtained from the analytical model, as illustrated in Fig.31. A linear regression analysis was performed on the dataset, and the slope of the best-fit line was taken as the effective gauge factor of the sensor.

The relationship can be expressed as:

$$\frac{V_{out}}{V_{in}} = GF \cdot \varepsilon + C \tag{3.6}$$

where the slope represents the gauge factor and C accounts for any offset due to measurement noise or initial imbalance in the Wheatstone bridge.

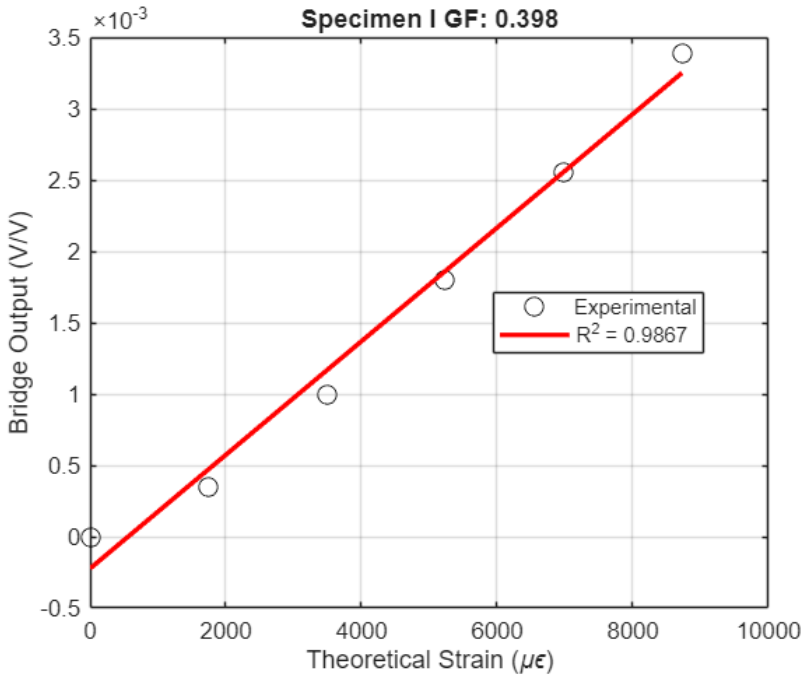

Fig. 31. Sensitivity Extraction of Sensor I - Tension

The calculated GF is lower than that of the conventional metallic strain gauges, which is attributed to the imperfect strain transfer within the printed sensor and certain uncertainties in the intrinsic property of the material.

Furthermore, since the strain was derived using an assumed modulus, any deviation between the nominal and actual stiffness of the printed specimen is inherently reflected in the calculated gauge factor.

Using the calibrated gauge factor, the experimental strain was calculated from the measured sensor output:

$$\epsilon_{exp} = \frac{V_{out}/V_{in}}{GF} \tag{3.7}$$

This provides a direct conversion from electrical response to mechanical strain.

To verify and validate the experimental results, a simulation was conducted using SolidWorks, where a static study of the specimen was performed. One end of the specimen was fixed, and a tensile load was applied at the opposite end. Material properties were defined using a non-conductive PLA datasheet, and strain values were extracted from the region corresponding to the sensor location.

The simulation set-up and results are shown in Fig.32. showed strong agreement with the theoretical predictions, with a slight underestimation observed across the load range. This deviation might be due to boundary condition simplifications and numerical discretisation.

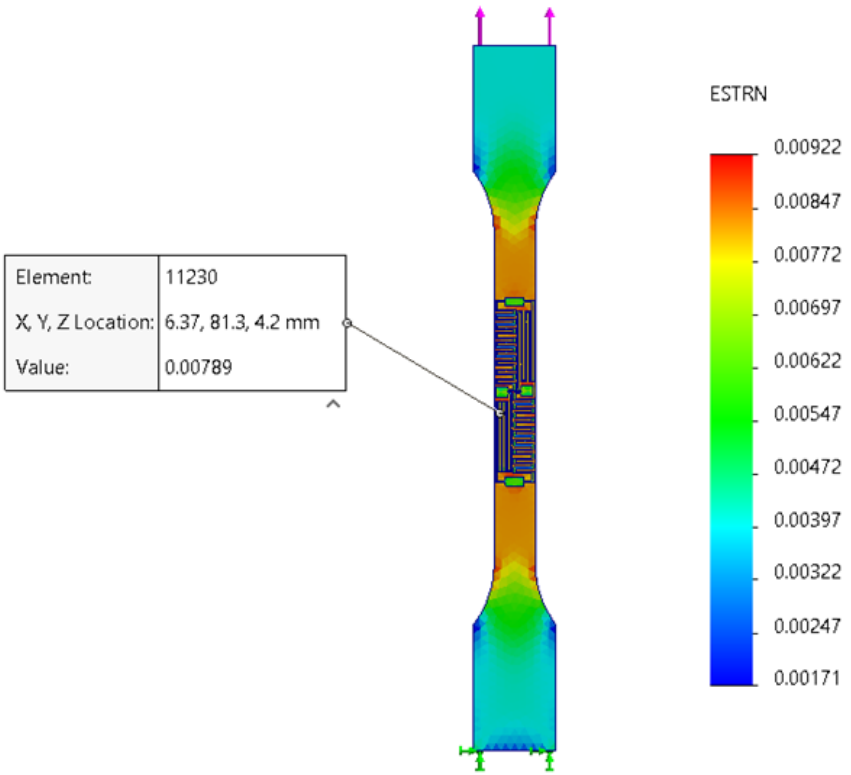

Fig. 32. Static Study of the specimen at 400 N

The results were then plotted against applied load to be comapared and characterised**.**

In Fig.33, all three approaches, analytical, experimental, and numerical, demonstrate a linear relationship between load and strain, which confirms the elastic behaviour within the tested range.

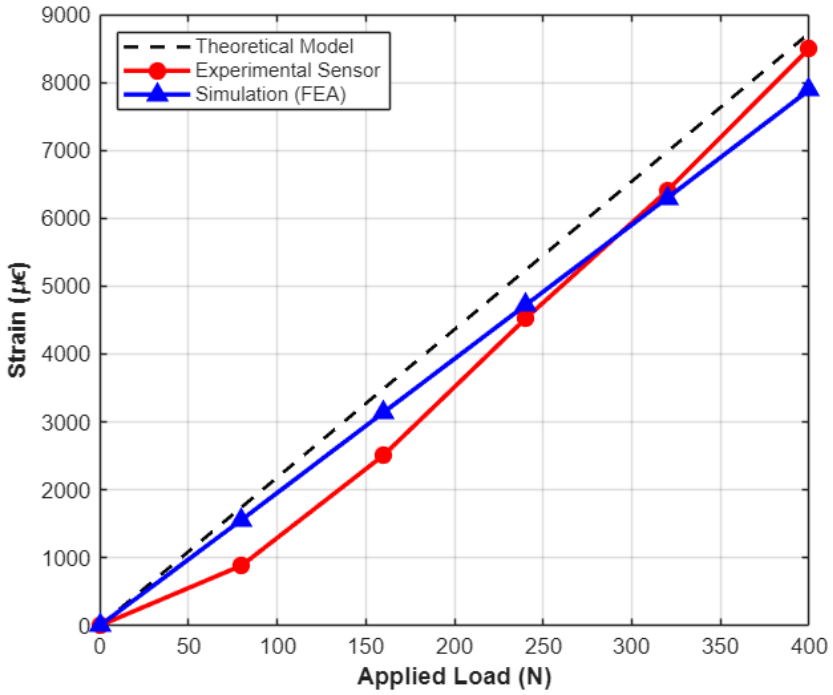

Fig. 33. Comparison - Strain vs. applied load for design layout I under tensile loading

The comparison showcases larger deviations in the experimental strain at lower load, which is attributed to the lower sensitivity and measurement noise. However, as the load increases, the values converge with the simulation and theoretical values.

At higher loads, strong agreement is observed between all three methods, confirming the validity of the analytical model, the reliability of the simulation, and the effectiveness of the sensor in capturing strain under tensile loading conditions.

3.1.4. Tensile analysis – design specimen II.

The behaviour of the second layout was evaluated over a load range of 0 -1200 N.

Since both layouts are tested under identical thickness and stress conditions and are expected to follow the same trend, the output vs load plot is not repeated to avoid redundancy.

The sensitivity of the second design layout is determined in the identical manner as the first layout using linear regression of the bridge output with respect to strain.

The extracted gauge factor from the regression plot, Fig.34, was 1.27.

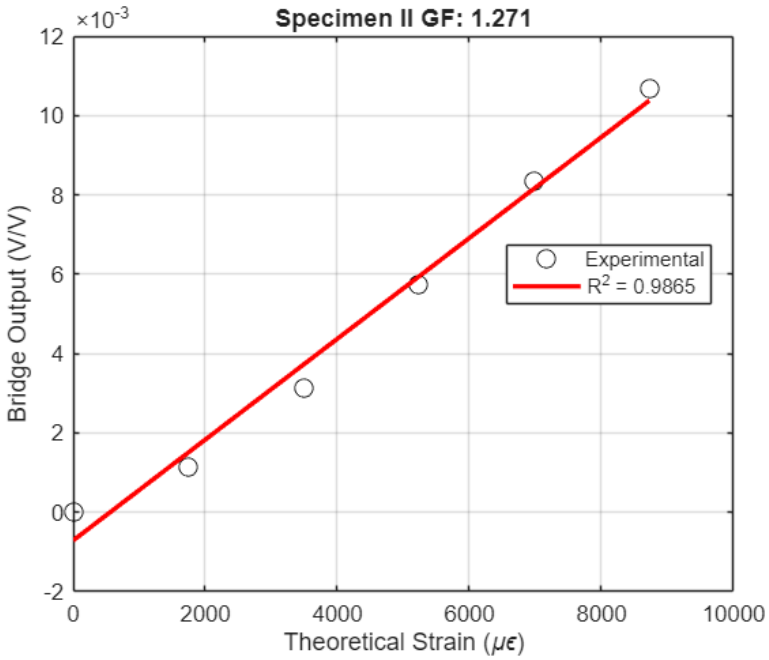

Fig. 34. Sensitivity Extraction of Sensor II – Tension

Layout II shows a substantial increase in sensitivity, which is attributed to the compact geometry of the bridge, which enhances strain utilisation and results in exhibiting a stronger electrical response.

Strain was evaluated using theoretical, experimental, and numerical approaches, consistent with the methodology established for Design Layout I. A corresponding finite element analysis was performed in SolidWorks to validate the results.

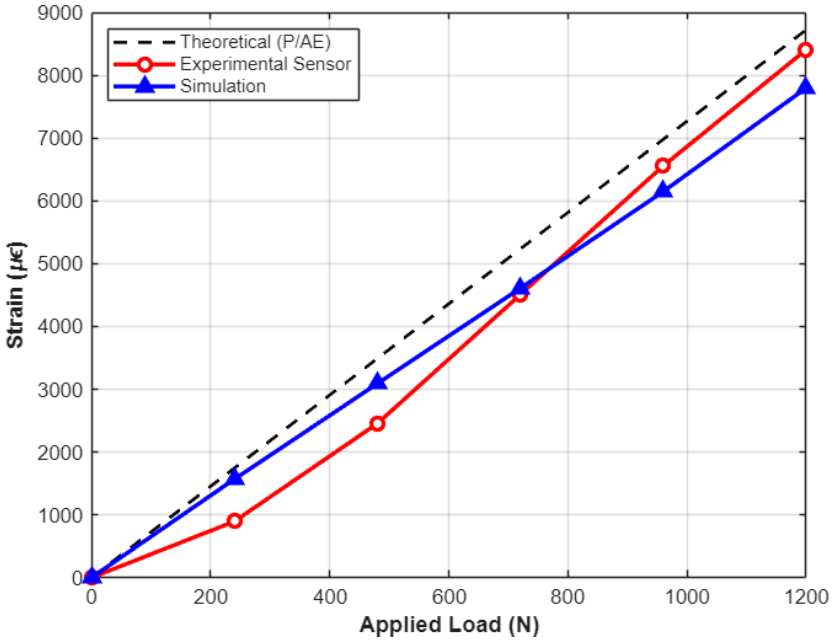

Fig. 35. Comparison - Strain vs. applied load for Design Layout II under tensile loading

In Fig.35, we can see that the experimental response exhibits an initial deviation at lower loads, where the measured strain is lower than both theoretical and simulated predictions up to approximately 600

N. This behaviour is attributed to mechanical seating effects and minor interfacial slip between the sensor and substrate, which are common in additively manufactured materials due to surface irregularities.

Beyond this region, the sensor response becomes highly linear and converges with both theoretical and simulation results at higher loads, indicating stable and reliable strain measurement once initial effects are overcome.

3.1.5. Performance comparison

A comparison of both sensor layouts confirms that each exhibits a linear relationship between output and strain, indicating consistent and stable behaviour.

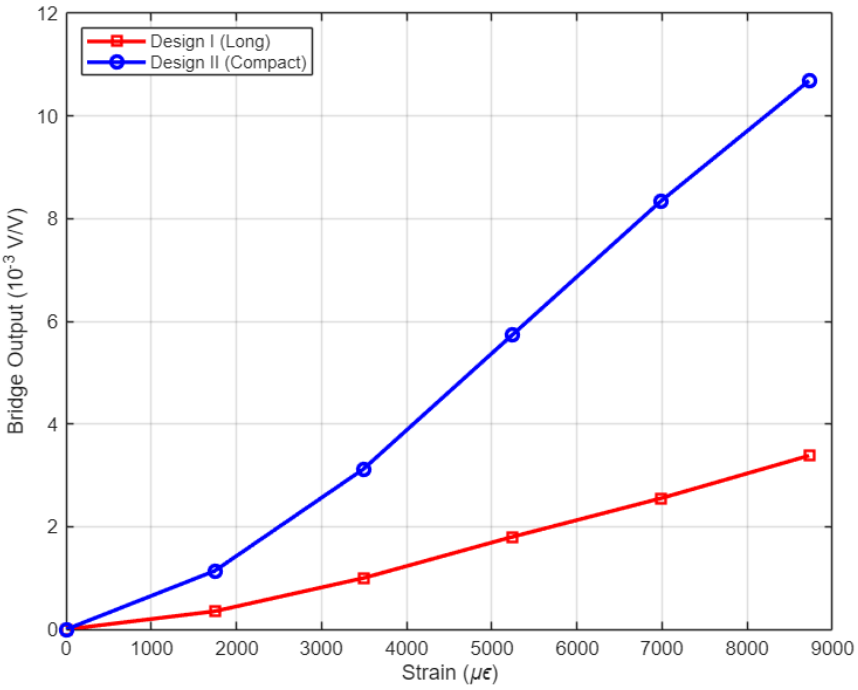

Fig. 36. Comparison between sensors (Output vs Strain)

According to Fig 36, Design Layout II constantly produces a significantly higher electrical output for the same strain level. For example, at approximately 8500 με:

- Design Layout I: 0.0034 V/V
- Design Layout II: 0.0107 V/V

This improvement is directly attributed to the sensor geometry. The compact full-bridge configuration in Design Layout II enables more efficient strain transfer and enhanced signal generation.

3.2. Three-point bending test

For the second loading case, three-point bending was employed to evaluate the response of the sensor under flexural loading, where strain is non-uniform and reaches a maximum at the outer surfaces. This loading condition closely represents real structural applications, such as UAV components, where bending dominates over pure axial loading.

Testing was conducted using a Tinius Olsen universal testing machine.

3.2.1. Experimental setup and load range

The experiments followed a standard three-point bending configuration (ISO 178) [29]. The support span of 64 mm was maintained in accordance with the span to thickness ratio of 16:4. The diameter of the support was 5 mm, which exceeds the thickness of the specimen to facilitate proper load distribution and also minimise local stress concentrations.

As depicted in Fig 37, a central load was applied at mid-span, while both load and displacement were recorded throughout the test.

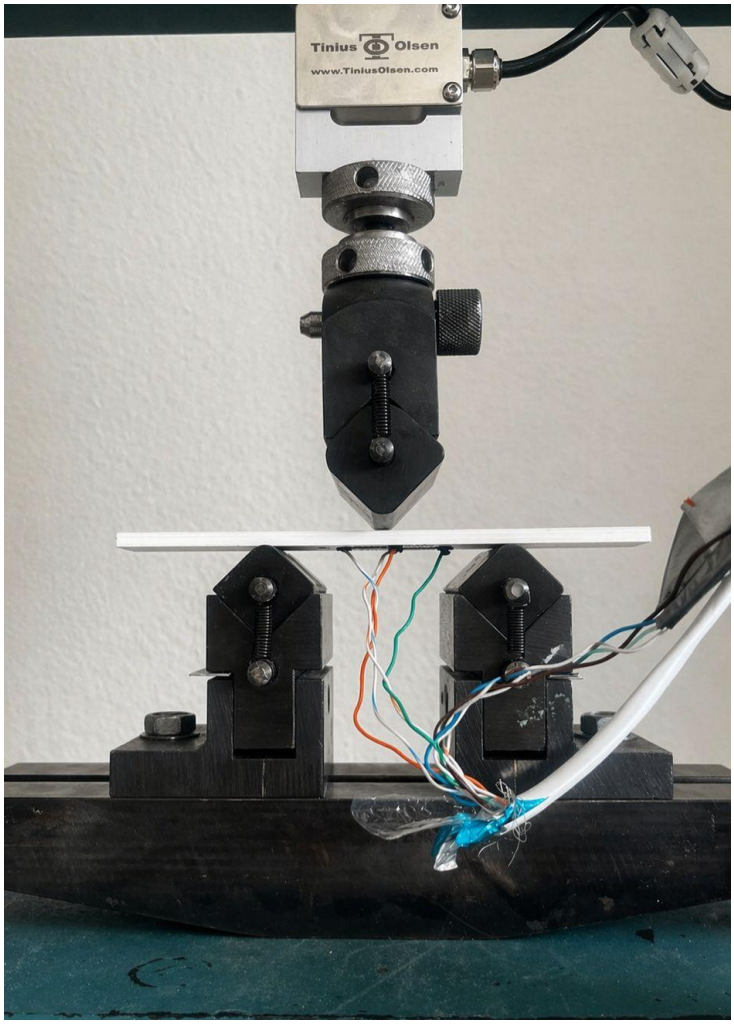

Fig. 37. Experimental set-up – three-point bending

The specimens were positioned with the sensor layer facing downward, opposite to the applied load direction. This ensured that the sensor was located at the bottom surface, where maximum tensile strain occurs during bending.

The load ranges were selected as follows:

- Specimen I (Width = 10 mm): Initially 0–10 N, extended to 24 N to improve sensor resolution
- Specimen II (Width = 30 mm): Initially 0–20 N, extended to 60 N to achieve measurable strain due to increased stiffness

3.2.2. Bending analysis – specimen I

The strain in Specimen I under three-point bending was evaluated using both analytical and experimental approaches. In addition, the sensor response was correlated to strain through gauge factor calibration.

For a simply supported beam subjected to a central load, the theoretical surface strain is given by:

$$\epsilon_{th} = \frac{3FL}{2bh^2E} \tag{3.8}$$

where F is the applied load, L is the support span, b is the specimen width, h is the thickness, and E is the Flexural modulus (2490 MPa). Substituting the specimen parameters at the maximum load $F = 24$ N, the theoretical strain is:

$\epsilon_{\text{th}} = 5783\ \mu\epsilon$

The mid-span displacement (δ) was recorded directly from the Tinius Olsen testing machine during the bending test.

The strain was then determined using:

$$\epsilon_{disp} = \frac{6h\delta}{L^2} \tag{3.9}$$

Using the measured displacement $\delta = 0.872$ mm, the experimental strain is calculated to be:

$\epsilon_{\text{disp}} = 5109\ \mu\epsilon$

This approach provides a direct geometric measurement of strain and avoids reliance on assumed material properties.

The gauge factor was determined by relating the measured electrical output to the corresponding strain.

- Using theoretical strain: $\text{GF}_{\text{th}} = 0.899$
- Using displacement strain: $\text{GF}_{\text{disp}} = 1.018$

The theoretical gauge factor ($\text{GF}_{\text{th}} = 0.899$) was derived under the assumption of a nominal flexural modulus of 2490 MPa [28]. In contrast, the experimentally obtained gauge factor ($\text{GF}_{\text{disp}} = 1.018$) reflects the actual mechanical response of the 3D-printed specimen.

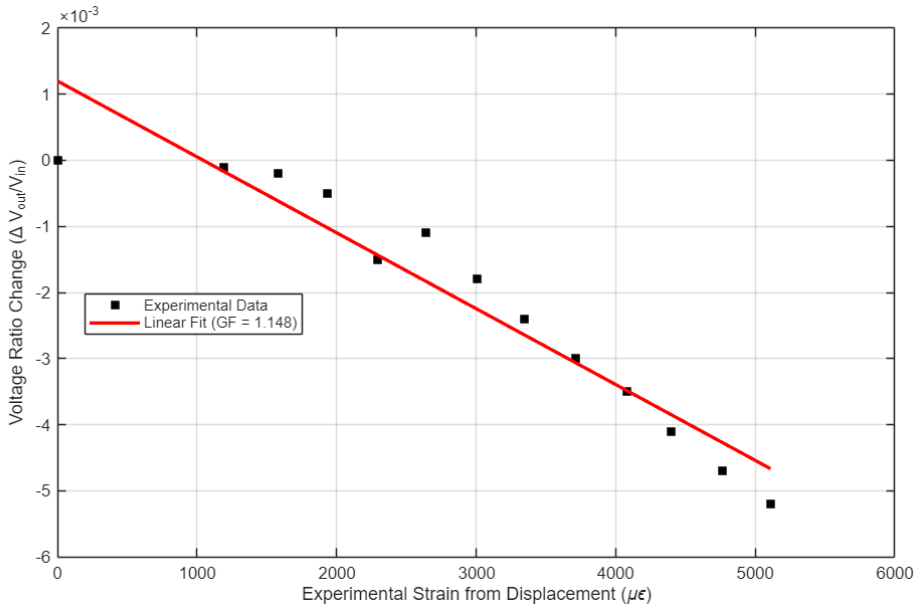

Fig. 38. Sensitivity extraction of specimen I - bending

The discrepancy between these values is attributed to a deviation in the effective stiffness of the material. The measured mid-span displacement (0.872 mm) was slightly lower than the theoretically predicted value (0.877 mm), indicating a stiffer structural response than initially assumed.

As seen in the comparison plot Fig.39. below, the theoretical curve follows a linear trend based on beam assumptions. The mechanical strain, obtained from displacement measured by the Tinius Olsen machine, follows a similar trend but is slightly lower at higher loads, indicating a stiffer actual response.

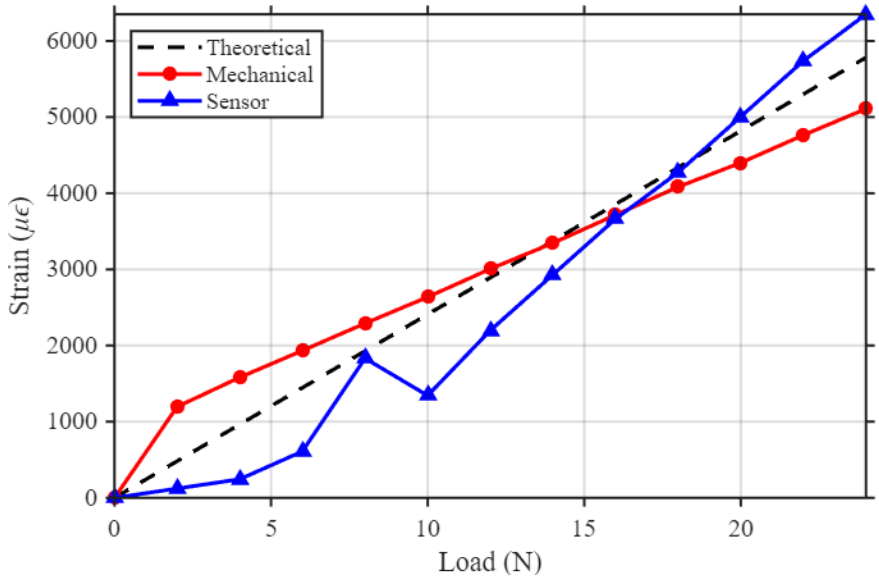

Fig. 39. Comparison - strain vs. applied load for design layout I under bending

The sensor response shows a noticeable spike around the initial loading range. This is likely due to specimen movement or slight instability in the setup, as no rigid clamping was used, combined with initial strain transfer effects.

Beyond this region, the sensor output becomes linear and aligns well with the mechanical strain, confirming stable behaviour. At higher loads, the sensor slightly overestimates strain, which may be attributed to local strain concentration and calibration sensitivity.

Overall, the sensor demonstrates reliable performance once the initial instability is overcome, with good agreement in the higher load range.

3.2.3. Bending analysis – specimen II

Strain was evaluated using displacement measurements obtained directly from the Tinius Olsen testing machine, following the methodology established for Specimen I.

At the maximum load of 60 N, the measured displacement ($\delta = 0.855$ mm) resulted in an experimental strain of 5010 με.

The corresponding theoretical strain, calculated using the nominal modulus ($E = 2490$ MPa), was 4819 με. The close agreement between these values indicates that the mechanical response of Specimen II aligns well with theoretical predictions.

The experimentally determined flexural modulus was 2395 MPa. This value is close to the nominal modulus (2490 MPa), suggesting that the wider specimen exhibits more consistent and predictable mechanical behaviour. This is likely due to the reduced influence of printing-induced variability across the larger cross-section.

The resulting gauge factors were:

- Theoretical GF: 1.32
- Experimental GF: 1.20

Unlike Specimen I, the experimental gauge factor is slightly lower than the theoretical value, reflecting improved agreement between predicted and measured strain.

The theoretical strain follows a linear trend based on beam theory. The mechanical strain, obtained from displacement measurements, closely follows this prediction, indicating that the specimen behaves in good agreement with the assumed material properties.

The sensor response shows a gradual increase with load but consistently underestimates strain at lower and mid-load levels. This behaviour is attributed to strain transfer limitations and interfacial compliance between the sensor and the substrate.

As the load increases, the sensor response becomes more linear and converges toward the mechanical strain. At higher loads, the agreement improves significantly, confirming stable and reliable sensor performance.

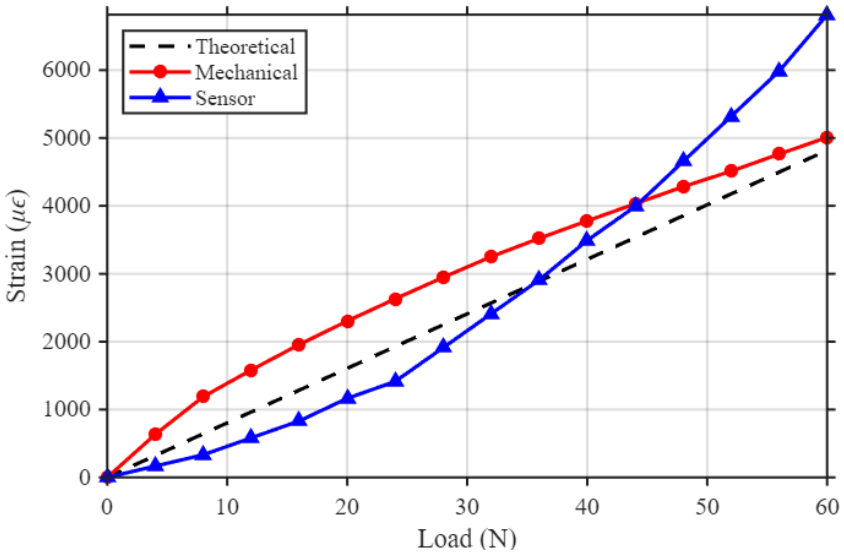

Fig. 40. Comparison - Strain vs. applied load for design layout II under bending

Overall, compared to Specimen I, the response is smoother with no sudden spikes, indicating improved stability of the setup and reduced influence of initial mechanical disturbances.

3.2.4. Discussion

Both layouts exhibit a consistent, approximately linear output with increasing strain, confirming stable piezoresistive behaviour. However, a clear distinction is observed in sensitivity and signal magnitude.

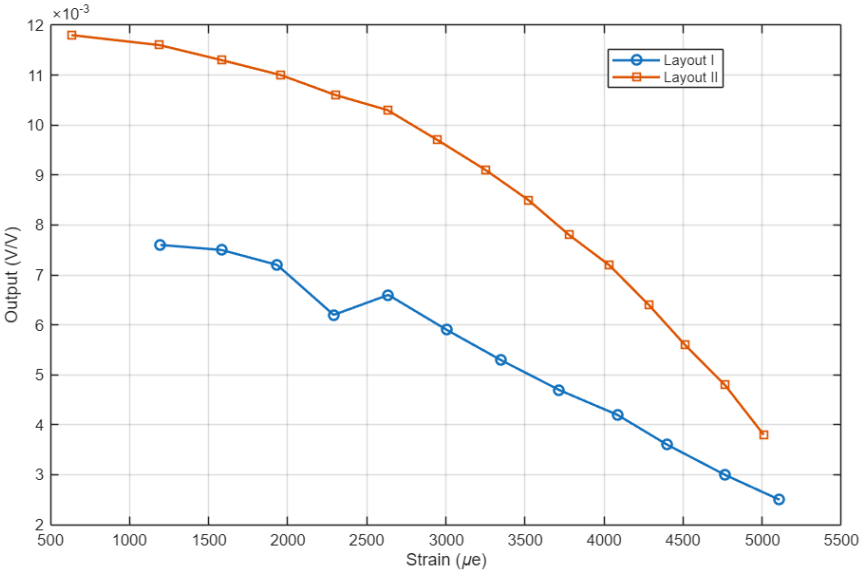

Fig. 41. Comparison between sensors (Output Vs Strain)

The improved performance of Design Layout II is attributed to its compact full-bridge configuration, which enhances strain utilisation across the sensing elements. In contrast, Layout I exhibits lower sensitivity due to less efficient strain transfer and a more distributed geometry.

Additionally, Layout I shows minor irregularities in response at intermediate strain levels, indicating localised inconsistencies such as non-uniform strain distribution or partial strain transfer. These effects are significantly reduced in Layout II, which demonstrates a smoother and more consistent response.

Overall, while both sensor designs provide reliable and linear behaviour, Design Layout II offers superior sensitivity and improved signal stability, making it the preferred configuration for strain-sensing applications.

4. Integration into UAV structure

A 13-inch FPV drone arm was selected for integration due to its structural characteristics and relevance to real-world applications. The arm behaves as a cantilever beam during operation, experiencing bending loads that generate measurable tensile and compressive strains along its length. This makes it suitable for evaluating the performance of the developed strain sensor under practical loading conditions. Based on the performance of both layouts, the second compact layout was selected to be integrated, given its superior performance.

4.1. CAD design and geometry preparation

The UAV arm was designed in the CAD software, ensuring that it is compatible with the standard FPV configurations while ensuring sufficient space for placing the sensors on it. The UAV arm was developed with an overall length of approximately 320 mm and a uniform cross-section of 30 mm × 5 mm.

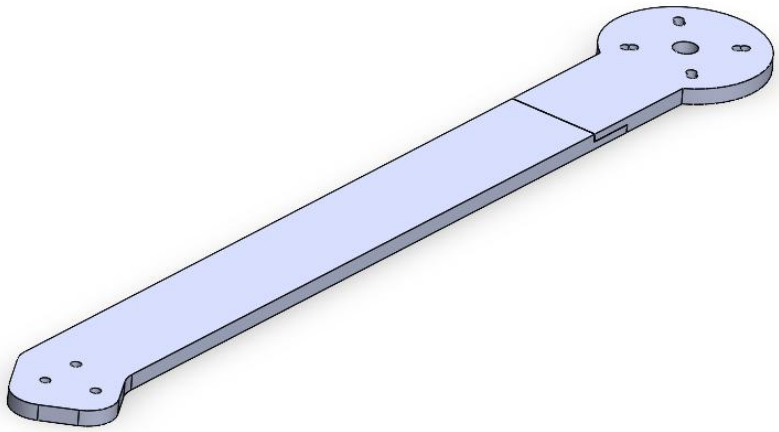

Fig. 42. CAD model of the UAV arm

Due to the build volume limitations of the available 3D printer, the arm was divided into two equal sections to enable fabrication. Each section was printed separately and subsequently bonded using adhesive to form the complete structure. This approach ensured manufacturability while maintaining the intended geometry for structural evaluation.

4.2. Sensor placement

Three sensors were incorporated onto the UAV arm to capture different loading conditions along its length. As seen in Fig 42, the sensors (A & B), closer to the fixed end and at mid-span, consisted of a conventional strain gauge configuration, intended to measure bending-induced tensile strain.

Finally, a third sensor, specifically designed at 45°, was placed toward the free end of the arm. The 45° sensor captures combined shear and normal strain components, providing indirect sensitivity to torsional effects.

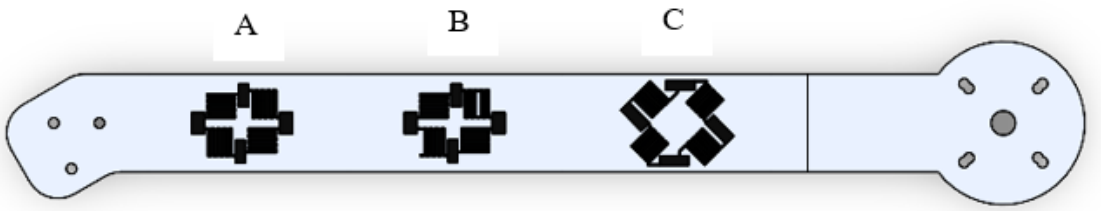

Fig. 43. Location of the sensors on the arm

The spacing between adjacent sensors was maintained at approximately 30 mm to ensure distinct measurement regions along the structure.

4.3. Manufacturing parameters

The UAV arm with integrated sensors was fabricated using FDM 3D printing.

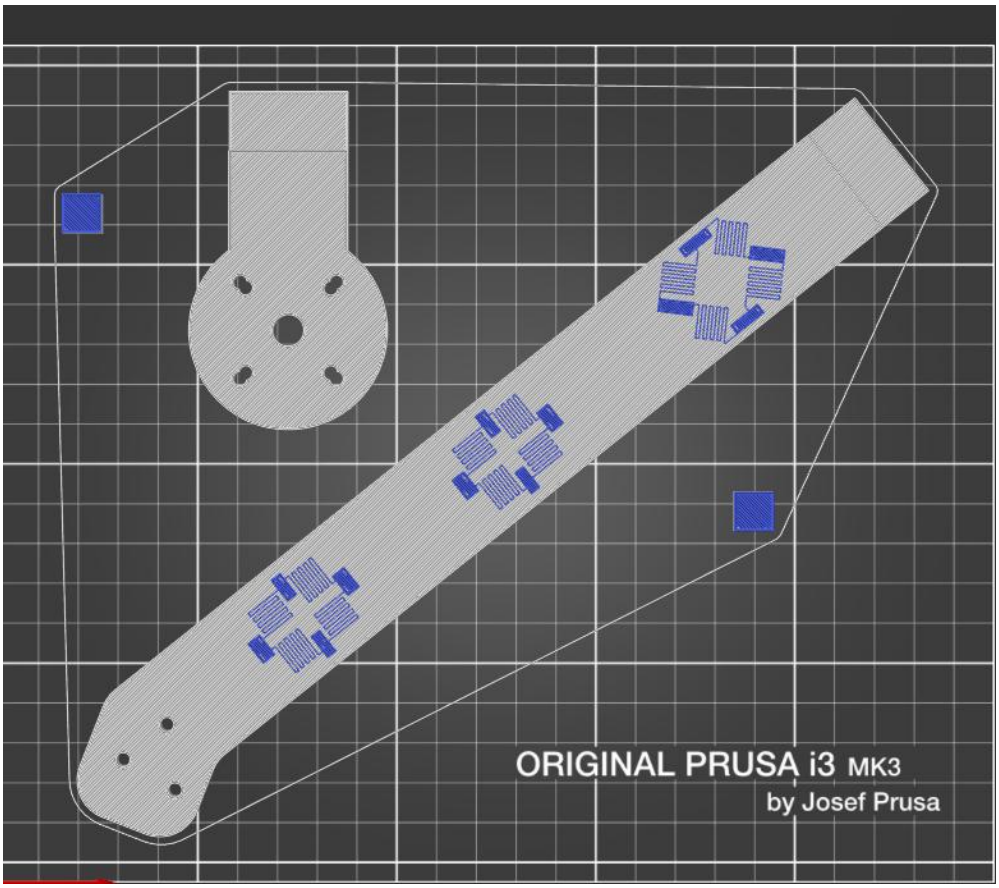

Fig. 44. Slicer window of the arm

The following parameters were used to ensure structural integrity and consistent sensor formation:

- Infill: 100%
- Extrusion multiplier: 1.04
- Nozzle temperature: 225°C

A manual filament change was implemented during printing to switch between structural (PLA) and conductive materials, enabling the formation of the integrated sensor within the arm.

4.4. Electrical integration

The electrical integration of the sensors on the UAV arm was performed using the same procedure described previously. Soldered connections with conductive composite material were used to establish continuity between the printed sensor tracks and external wiring.

The sensors were interfaced with the NI 9237 module within the NI cDAQ-9173 chassis, with data acquisition carried out in MATLAB.

4.5. Structural testing of UAV arm - bending test

4.5.1. Experimental setup

The bending behaviour of the UAV arm was evaluated using a cantilever loading configuration. One end of the arm was rigidly fixed to a table to simulate a fixed support condition.

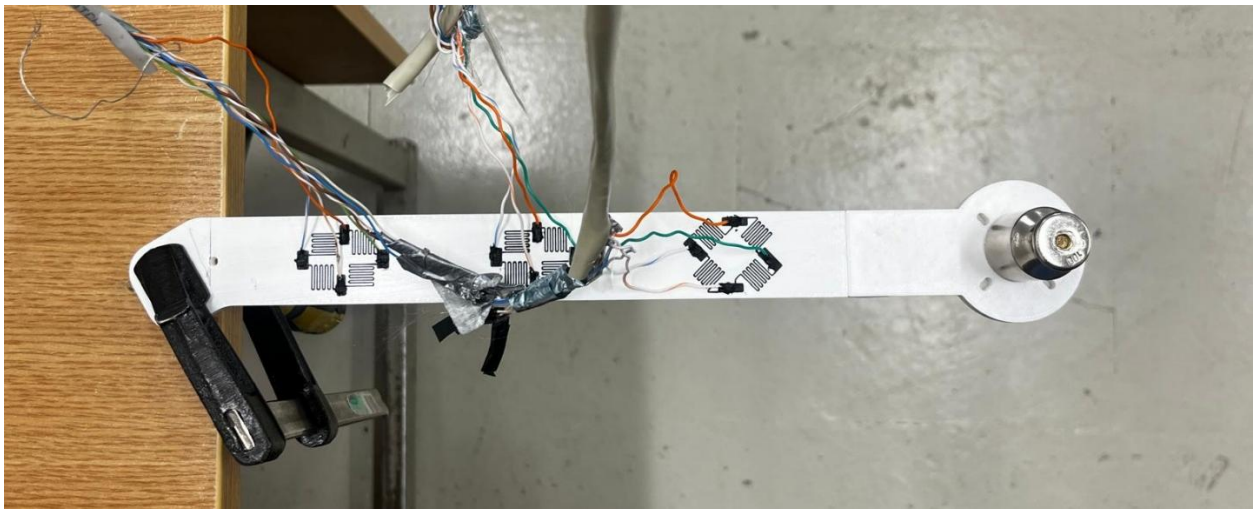

Fig. 45. Experimental Setup of the arm under bending

Loads were applied at the free end of the arm, corresponding to the motor mounting location. Calibrated masses of 20 g, 50 g, 100 g, and 200 g were applied.

4.5.2. Experimental results

The electrical response of all three sensors under bending load is shown in Fig.46. The sensor located near the fixed end (Sensor A) showcases the greatest change in output as the load increases, conveying that this location experiences maximum strain. The middle sensor shows a similar but reduced response. The torsion sensor shows very minimal variation, confirming that it is indifferent to bending-induced strain.

The NI 9237 module has a noise floor of approximately 30 nV/V RMS, which is several orders of magnitude below the measured signal levels, confirming that the recorded outputs represent genuine strain responses [30].

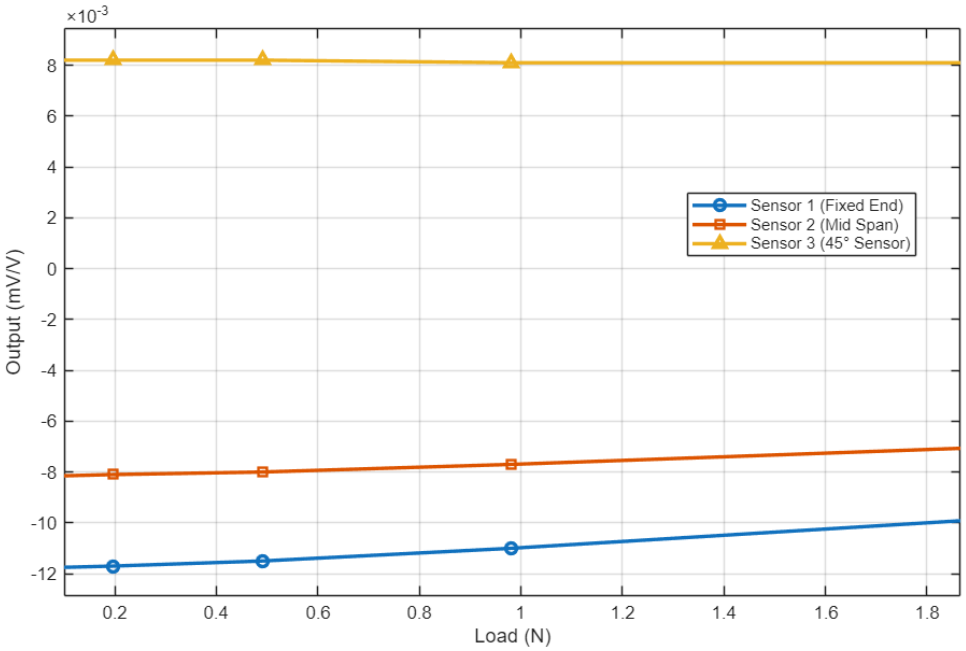

Fig. 46. Bridge output vs. applied load

The observed experimental trends are consistent with theoretical predictions based on cantilever beam behaviour, where strain is highest near the fixed support and decreases toward the free end. The negligible response of the torsion sensor further supports its specificity to torsional loading rather than bending.

The UAV arm was modelled as a cantilever beam subjected to a point load at the free end. The theoretical strain at different sensor locations was calculated using classical beam theory.

The bending moment at a given sensor location is expressed as:

$$M = F \cdot (L - x) \tag{4.1}$$

where F is the applied load (N); L is the total length of the arm (m); x is the distance of the sensor from the fixed end (m).

The normal strain at the outer surface of the beam is given by:

$$\varepsilon(x) = \frac{M(x) \cdot y}{EI} \tag{4.2}$$

For a rectangular cross-section, the second moment of area is:

$$I = \frac{bh^3}{12} \tag{4.3}$$

Substituting the bending moment into the strain equation:

$$\varepsilon_{theo} = \frac{F(L - x)(h/2)}{EI} \tag{4.4}$$

This expression was used to calculate the theoretical strain at each sensor location. Following which the gauge factor was calibrated to be 1.07.

A finite element analysis (FEA) was also conducted using SolidWorks Simulation to obtain strain distribution along the UAV arm under applied loading conditions.

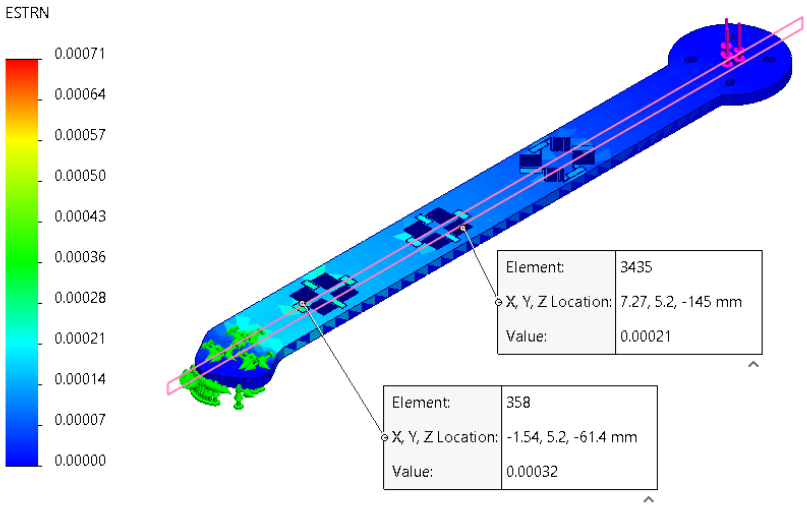

Fig. 47. Static study of the arm when F = 0.196 N

These simulation results were used as a reference to validate both the analytical beam theory and the output-based strain calculations.

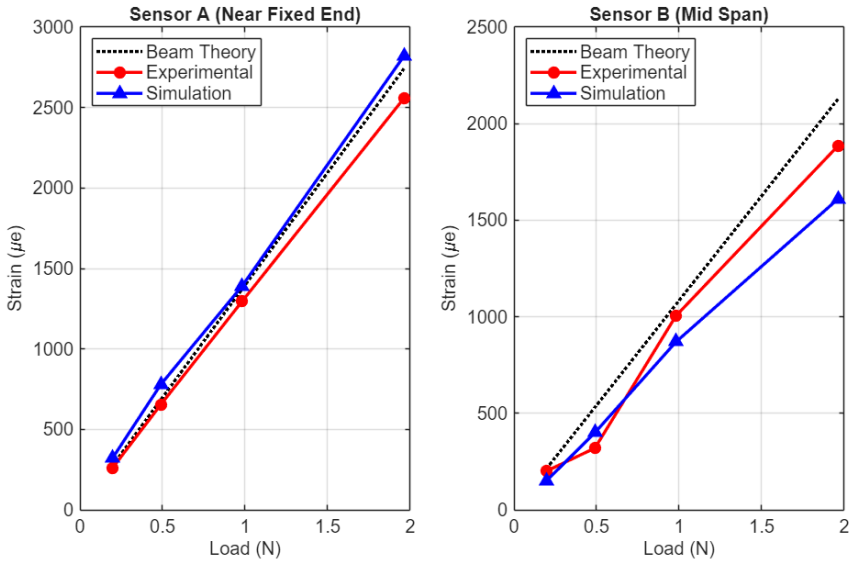

Fig. 48. Comparison - strain vs. applied load for sensor A & B

For Sensor A, all three methods exhibit a linear increase in strain with increasing load, indicating elastic behaviour of the structure. The analytical beam theory predicts the highest strain values, followed by the finite element simulation, while the experimental results show slightly lower values.

For Sensor A, all three methods of strain estimation increase with load, showcasing an elastic behaviour. While the analytical beam theory predicts the highest values, the simulation and experimental values closely follow. However, the experimental values underestimated the strain slightly.

At Sensor B, a similar linear trend is observed; however, the deviation between the three methods is more pronounced. The analytical model significantly overestimates strain, while the simulation predicts lower values. The experimental results lie between the two, showing better agreement with simulation than with beam theory.

It is important to take into consideration that the UAV arm was fabricated in two separate parts and bonded together using an adhesive. The bonded interface might have introduced localised stiffness variation and affected the load transfer. Such effects are more noticeable away from the fixed end, which helps explain the larger discrepancies observed at Sensor B.

The experimental strain shows error decreasing at higher loads and remaining within approximately 10% for Sensor A and 15–20% for Sensor B.

4.6. Structural testing of UAV arm - torsional test

A torsional offset configuration was implemented to evaluate sensor response under combined loading. A rigid peg extended 100 mm perpendicular to the UAV arm, creating a moment arm about the longitudinal axis as seen in Fig.49.

The combined mass of the offset hardware and fasteners was 36.18 g, introducing a constant preload across all test cases. Additional weights were applied vertically at the tip of the offset arm, generating both a bending moment (M) and a torsional moment (T).

Sensor C, oriented at 45°, was used to capture the resulting multi-axial strain state, combining axial and shear components.

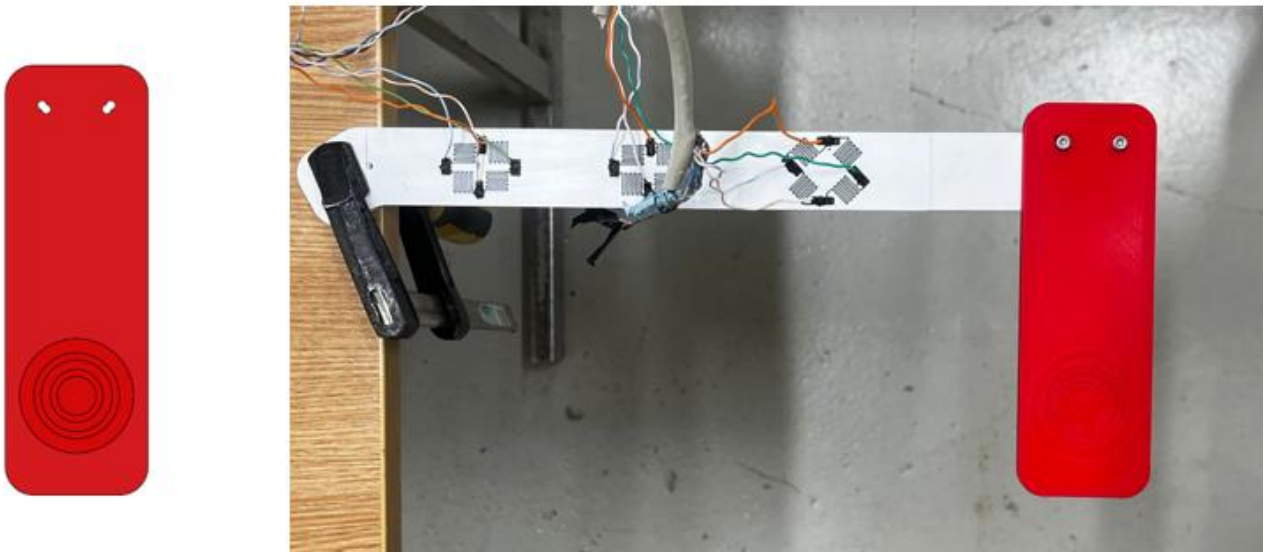

Fig. 49. Experimental Set-up of the arm under bending and torsion

The remaining experimental setup, including boundary conditions and data acquisition procedure, was identical to that used in the bending test.

The strain at Sensor C was obtained by superimposing bending and torsional contributions:

$$\epsilon_C = \frac{\epsilon_x(1-\nu)}{2} + \frac{\gamma}{2} \tag{4.4}$$

Including the hardware mass, the load case (20 g applied) corresponds to a total mass of 236.18 g (0.551 N). The resulting strain components at x = 160 mm are summarised below:

Table 5. Theoretical strain components at Sensor C location (x = 160 mm) under combined bending and torsional loading

Component	Calculation	Strain Value (με)
Bending	$\frac{\epsilon_x(1-\nu)}{2}$	92.0
Torsion	$\frac{\gamma}{2}$	133.0
Total	Sum	**225.0**

A linear regression analysis was performed on the experimental data collected during the offset loading test. By accounting for the 36.18 g initial hardware mass in the theoretical model, a gauge factor of 0.97 was derived.

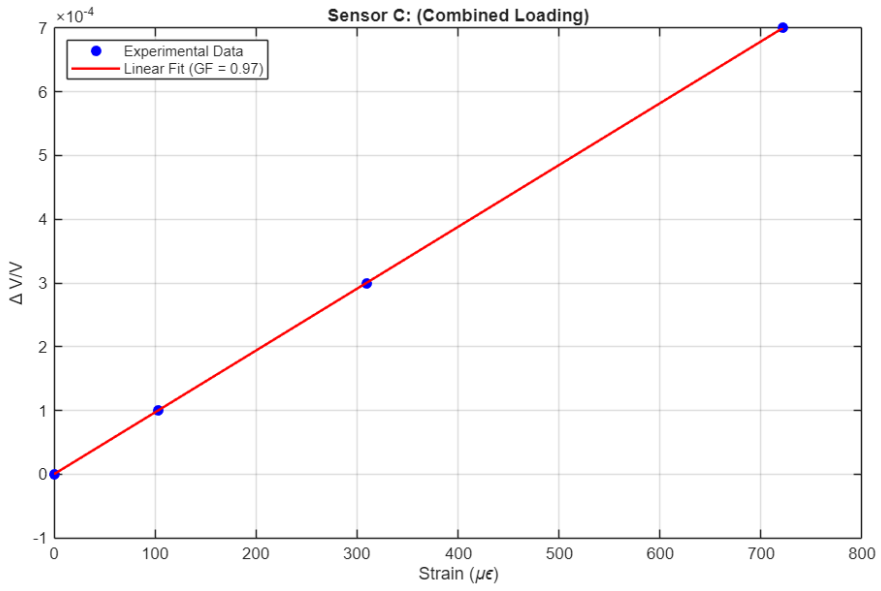

Fig. 50. Sensitivity extraction of sensor C (45°)

A GF of 0.97 indicates high electromechanical efficiency for an additive-manufactured sensor. Notably, this value is consistent with the longitudinal sensors (Sensors A and B), which typically exhibit GF values near 1.0. The slight reduction in sensitivity for Sensor C is expected due to the 45° print raster orientation, which introduces a different conductive network path relative to the primary strain axis.

A static study was once again performed under the same loading conditions. The plate was mated to the arm, and force was applied as demonstrated in Fig.51 below.

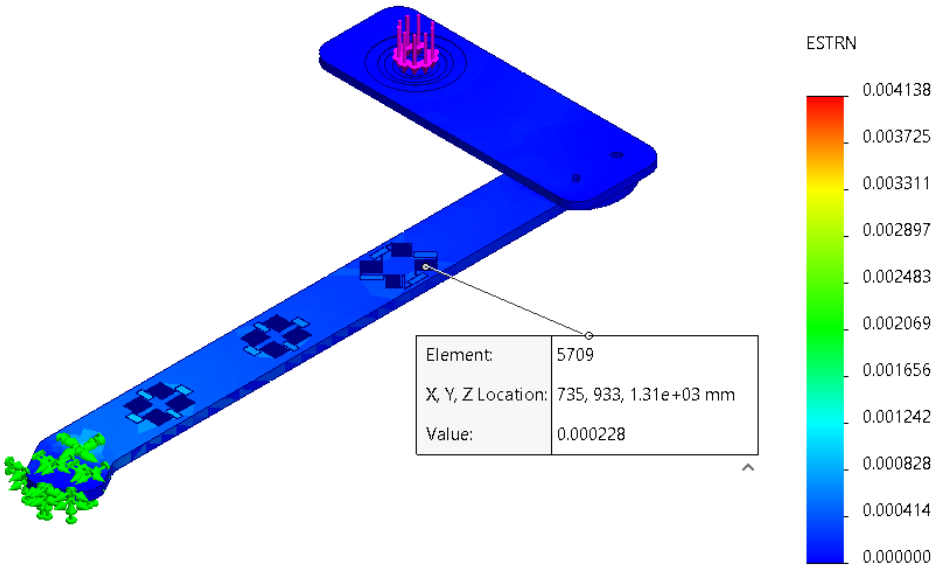

Fig. 51. Static study of the arm with the torsion plate at F = 0.551 N

A comparison study of the results has been performed, where the measured strain is plotted against the applied load.

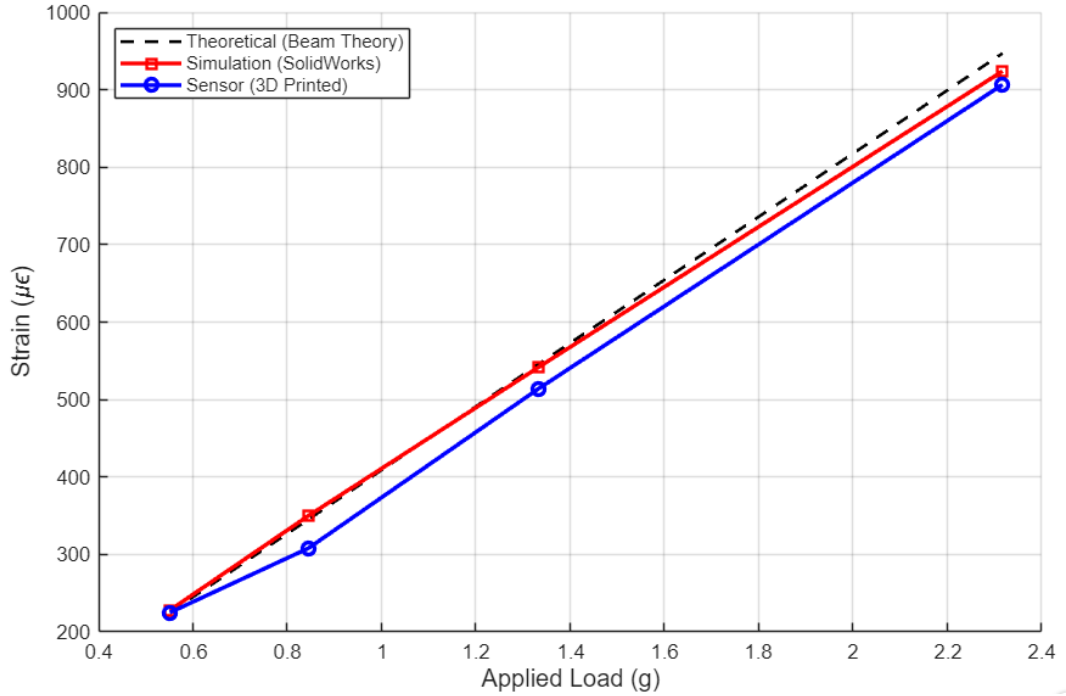

Fig. 52. Comparison - strain vs. applied load for sensor C

All three approaches exhibit a linear increase in strain with applied load as seen in Fig.52, confirming elastic behaviour under the tested range. The simulation results closely follow the theoretical prediction, indicating that the numerical model accurately captures the structural response.

The sensor-derived strain shows good agreement with both theoretical and simulation results, with a slight underestimation observed across all load levels. This deviation is attributed to strain transfer losses and interfacial compliance between the printed sensor and substrate, as well as inherent material anisotropy in the 3D-printed structure.

At the maximum load, the experimental strain remains within a small deviation from the theoretical value, demonstrating that the sensor provides reliable and consistent measurements under combined loading conditions.

4.7. Discussion

The output of the integrated strain sensor manufactured using additive manufacturing in a UAV arm clearly depicted that it is indeed viable and capable of capturing meaningful strain response under both bending and torsional loading. The results followed the expected mechanical behaviour as predicted using the classic cantilever beam theory and finite element analysis. The sensing approach was deemed fundamentally sound.

However, the performance of the system critically depends on the sensor's fabrication and not just on structural mechanics.

The sensor location also plays a vital role in the observed differences. As seen, Sensor A strongly agrees with the theoretical prediction (within ~10%) while Sensor B shows a discrepancy (15-20%) which could not be explained by structural theory alone. It is possible that the bonded variation introduced stiffness and minor inconsistencies through the sensing element during fabrication, resulting in strain loss.

Another key limitation lies in strain transfer efficiency. This leads to systematic underestimation of strain, as observed across both bending and torsional tests. From an application standpoint, this means the technology is suitable for embedded sensing in lightweight structures such as UAV arms, where low cost, geometric integration, and weight reduction are prioritised over high-precision strain measurement. However, for applications requiring high accuracy or standardisation, the current approach would require tighter process control or calibration procedures.

Overall, the system is reliable for capturing strain trends and relative changes, but its accuracy is limited by manufacturing consistency. Improving fabrication control is therefore more critical than refining the mechanical model.

Conclusions

1. Upon reviewing current structural health monitoring technologies, it was established that conventional strain sensing methods present significant limitations for integration into lightweight and geometrically complex structures, due to their dependence on surface bonding, rigid form factors, and extensive wiring requirements. This identified additive manufacturing as a promising alternative approach, enabling sensing elements to be directly fabricated within or onto structural components at low cost and with high geometric flexibility.
2. A 3D printed strain sensor was successfully designed and fabricated using FDM technology with Protopasta Conductive PLA, selected over Filaflex Conductive TPU following comparative material evaluation. The printed Protopasta sensor demonstrated a pad-to-pad resistance of approximately 273–275 kΩ, significantly lower than the Filaflex sensor, which exhibited resistance values of approximately 1.1 MΩ. Two full Wheatstone bridge layouts were designed and fabricated: a longitudinal configuration with a measured bridge resistance of approximately 137 kΩ and a compact full-bridge configuration with a measured resistance of approximately 100 kΩ, compared to a predicted value of 147 kΩ. The deviation is attributed to track overlap and fabrication effects inherent to the compact geometry.
3. An experimental setup was developed and validated for evaluating the sensor's electrical response under mechanical loading, utilising a Tinius Olsen universal testing machine for load application and an NI 9237 strain input module for data acquisition. Conductive PLA thermal bonding was identified as the most reliable electrical connection method, yielding stable and repeatable measurements. Temperature drift evaluation revealed that the compact Layout II demonstrated improved thermal stability due to its symmetric bridge geometry.
4. Both sensor layouts demonstrated clear piezoresistive behaviour under tensile and three-point bending loading conditions. Under tensile loading, the compact Layout II achieved a gauge factor of 1.27, compared to 0.398 for the longitudinal Layout I. Under three-point bending, Layout II achieved a gauge factor of 1.20 based on displacement-derived strain, compared to 1.018 for Layout I. The higher sensitivity of Layout II is attributed to its compact full-bridge geometry, enabling more efficient strain utilisation. Experimental results showed good agreement with analytical beam theory and finite element predictions across both loading conditions, with convergence observed at higher load levels beyond the initial seating region.
5. The compact Layout II sensor was successfully integrated into a 3D printed UAV arm and evaluated under bending and torsional loading conditions. Under both loading conditions, a gauge factor of ~1 was extracted. The sensors captured the expected cantilever strain distribution, with experimental values within approximately 5-20% of theoretical predictions. Overall, the findings confirm the practical feasibility of additively manufactured strain sensors for structural state monitoring in lightweight UAV structures.

List of references

1. ARIFFIN, A. H.; MOHAMAD, Z.; MAHZAN, S. A brief review on structural health monitoring sensor technology in civil and aviation technology applications. Penerbit UTHM, 2020.
2. CHAMBERS, J. T.; WARDLE, B. L. Durability testing of an aircraft structural health monitoring system, 2006.
3. SHAMEEM, B.; EBNA, M.; BAUSE, M.; KUBERRY, P. FEDSM2016-7506, finite element approximation of the extended fluid-structure interaction (EXFSI) problem.
4. HASSANI, S.; DACKERMANN, U. A systematic review of advanced sensor technologies for non-destructive testing and structural health monitoring. Sensors, 2023. DOI 10.3390/s23042150.
5. PENG, H.; WANG, B.; NING, Y.; CAO, S.; LIU, M. Strain gauge location optimization for operational load monitoring of an aircraft wing using an improved correlation measure. Aerospace, 2024. DOI 10.3390/aerospace11100823.
6. STEINWEG, D. M.; HORNUNG, M.; BOLLER, C. Cost and benefit of structural health monitoring in commercial aviation.
7. PERERA, R. Advanced sensing technologies in structural health monitoring and its applications. Sensors, 2025.
8. MARDANSHHAI, A.; SREEKUMAR, A.; YANG, X.; BARMAN, S. K.; CHRONOPOULOS, D. Sensing techniques for structural health monitoring: a state-of-the-art review on performance criteria and new-generation technologies. Sensors, 2025, vol. 25, art. no. 1424. DOI 10.3390/s25051424.
9. PIEZO DIRECT. Understanding unimorphs: a deep dive into piezoelectric technology [online]. Available from: https://piezodirect.com/understanding-unimorphs-a-deep-dive-into-piezoelectric-technology.
10. MEEHAN, R. E.; CONNOR, J. J. Technology and application of structural health monitoring in bridges, 2011.
11. KURNYTA, A.; ZIELINSKI, W.; REYMER, P.; DRAGAN, K.; DZIENDZIKOWSKI, M. Numerical and experimental UAV structure investigation by pre-flight load test. Sensors, 2020. DOI 10.3390/s20113206.
12. PRASAD, R. Overview of strain gauge and its various applications. International Journal of Engineering and Applied Sciences, 2023, vol. 10, no. 9, pp. 1–5. ISSN 2394-3661.
13. MUNASINGHE, N.; WOODS, M.; MILES, L.; PAUL, G. 3-D printed strain sensor for structural health monitoring. In: Proceedings of the IEEE Conference on Additive Manufacturing and Smart Structures. IEEE, 2019.
14. MAURIZI, M.; SLAVIČ, J.; CIANETTI, F.; JERMAN, M.; VALENTINČIČ, J. et al. Dynamic measurements using FDM 3D-printed embedded strain sensors. Sensors, 2019. DOI 10.3390/s19143167.
15. QU, J.; WU, Q.; CLANCY, T.; FAN, Q.; WANG, X.; LIU, X. 3D-printed strain-gauge micro force sensors. IEEE Sensors Journal, 2020, vol. 20, no. 13, pp. 6971–6978. DOI 10.1109/JSEN.2020.2976508.
16. HOFFMANN, K. Applying the Wheatstone bridge circuit.
17. ŞTEFĂNESCU, D. M. Strain gauges and Wheatstone bridges – basic instrumentation and new applications for electrical measurement of non-electrical quantities. Bucharest: Romanian Measurement Society.

18. İRSEL, G. Research on electrical strain gages and experimental stress analysis: case study for a full Wheatstone bridge. Dicle Üniversitesi Mühendislik Fakültesi Mühendislik Dergisi, 2021.
19. CHADDA, R.; DALI, O. B.; LATSCH, B.; SUNDARALINGAM, E.; KUPNIK, M. 3D-printed strain gauges based on conductive filament for experimental stress analysis.
20. KOUVATSOS, T.; PAGONIS, D. N.; IAKOVIDIS, I.; KALTSAS, G. Towards a 3D printed strain sensor employing additive manufacturing technology for the marine industry. Sensors, 2024. DOI 10.3390/s24154908.
21. LATI INDUSTRIA TERMOPLASTICI S.P.A. LATI3DLab: new conductive compounds for high performance 3D printing [online]. Available from: https://lati.com/en/lati3dlab-new-conductive-compounds-for-high-performance-3d-printing/.
22. MULTI3D LLC. Electrifi conductive filament [online]. Available from: https://www.multi3dllc.com/product/electrifi/.
23. AHMED, S.; ARTHUR, E. G.; OBRZUT, T.; SHERGILL, R.; WILLIAMS, A. et al. A comparative study of conductive 3D printing filaments for electrochemical sensing applications pretreated by alumina polishing, electrochemical activation, and electrodeposition of Au nanoparticles. ACS Applied Materials and Interfaces, 2025.
24. BADR, J.; MAHFOUD, E.; VILLAIN, G.; BALAYSSAC, J.; PALMA LOPES, S. et al. Temperature effect on electrical resistivity measurement using an embedded sensor to estimate concrete water content. Sensors, 2022. DOI 10.3390/s22186896.
25. PAUN, M.; SALLESE, J.; KAYAL, M. Temperature considerations on Hall effect sensors current-related sensitivity behaviour. Sensors and Actuators A: Physical, 2013. DOI 10.1016/j.sna.2013.10.015.
26. PROTO-PASTA. Conductive PLA [online]. Available from: https://proto-pasta.com/products/conductive-pla.
27. RECREUS. FilaFlex Conductivo [online]. Available from: https://recreus.com/en/products/filaflex-conductivo?variant=45921625833731.
28. PROTO-PASTA. Material Data Table [online]. Protoplant, makers of Protopasta, n.d. Available from: https://proto-pasta.com/pages/material-data-table.
29. LITHUANIAN STANDARDS BOARD. Plastics — Determination of flexural properties (ISO 178:2019) (2019-07-31 ed.). Vilnius: Lithuanian Standards Board, 2019. Available from: view.elaba.lt.
30. NATIONAL INSTRUMENTS. NI USB-9237 User Guide and Specifications: 4-Channel, 24-Bit Half/Full-Bridge Analog Input Device. Austin, Texas: National Instruments Corporation, 2007. Available from: ni.com/manuals)